Geochimica et Cosmochimica Acta 393 (2025) 254–267

Contents lists available at ScienceDirect

Geochimica et Cosmochimica Acta

journal homepage: www.elsevier.com/locate/gca

Quantifying the impacts of exogenous dust inputs to the critical zone using reactive transport modeling

Celia Aranda Reina [a,b], Julien Bouchez [b], Jennifer L. Druhan [a,b,*]

[a] Department of Earth Science and Environmental Change, University of Illinois Urbana-Champaign, Urbana, IL, 61801, USA
[b] Université Paris Cité, Institut de Physique du Globe de Paris, CNRS, Paris, 75005, France

ARTICLE INFO

Associate editor: Jiu bin Chen

Dataset link: http://www.hydroshare.org/resource/c5411ee6e1f54b9f9c7beaa9263f6969

Keywords:
Critical Zone
Dust deposition
Reactive transport models
Weathering rates

ABSTRACT

In upland watersheds, depletion of essential nutrients due to physical erosion and chemical weathering can be compensated by exogenous inputs such as aeolian dust deposition. However, it remains an outstanding challenge to describe the impacts of dust on the reaction rates that produce weathering profiles and how this cascades into ecosystem function and water chemistry. As increasingly intense and episodic periods of drought and aridity are promoted by a warming climate, the role of dust production and deposition in Critical Zone structure and function requires improved modeling techniques to facilitate rigorous quantification and prediction. Here we present a newly developed process-based reactive transport framework by modifying the open-source CrunchTope software in order to quantitatively interpret the impacts of dust deposition and solubilization in stream water chemistry, regolith weathering rates, and ecosystem nutrient availability. We describe two simulations: (1) a generic model demonstrating a simplified system in which bedrock uplift and soil erosion occur in tandem with solid phase dust deposition at the land surface; (2) a case study based on a small (0.54 km^2) upland Mediterranean watershed located on Mont Lozère in the National Park of Les Cévennes, France. In the absence of an exogenous dust input, long-term field observations of calcium in stream water, rain, soil, and plant samples cannot be produced by reactive transport simulations of the weathering profile. By adding a carbonate-bearing depositional input consistent with the composition of Saharan dust, both stream water chemistry and elemental mass-transfer coefficients in the soil profile better align with field observations, suggesting that dust has become a significant input to this field site in the last ~10 ka. Over this period, the deposition of exogenous carbonates has introduced far more calcium into the system than what could be supplied by the Ca-poor granitic bedrock. This highly soluble carbonate also limits the reactive potential of infiltrating precipitation, ultimately inhibiting chemical weathering rates and hence the component of elemental export fluxes derived from local bedrock.

1. Introduction

In landscapes that are highly weathered or erosive, or where bedrock is inherently deficient in a necessary element, exogenous deposition of aerosols and dust can offer vital mineral-derived nutrient sources fundamental to ecosystem health and primary productivity (Aciego et al., 2017; Chadwick et al., 1999; Pett-Ridge et al., 2009b; Soderberg and Compton, 2007; Dessert et al., 2019). In the Hawaiian Islands, Asian dust provides more base cations than the basaltic bedrock in soils older than 100,000 years, preventing what would otherwise be a calcium limitation to plant growth in these sites (Chadwick et al., 1999). The granitic watershed of Río Icacos in Puerto Rico is highly weathered, and an estimated 99% of the Ca and Sr in the bedrock has leached out (Pett-Ridge et al., 2009a). Since the last glacial period, relatively constant dust fluxes from the Saharan desert have become a major source of these nutrient elements to the soils and ecosystems in the Caribbean (Pett-Ridge et al., 2009b; Xu et al., 2022). Highly erosive montane forest ecosystems in the Southern Sierra Nevada (California, USA) have relied on dust as a source of rock-derived nutrients for the last million years, and presently this is the primary supply of phosphorus to these environments (Aciego et al., 2017).

Such exogenous elemental supplies to a landscape are often revealed through characteristic shallow excursions in mass-transfer coefficients across a given soil profile (Anderson et al., 2002; Brimhall and Dietrich, 1987). Where exogenous inputs are significant, the "parent" material composition is not simply bedrock, but requires constraint of some weighted average of the geochemical composition of dust and local lithology based on their relative contributions to the soil (Lawrence

* Corresponding author at: Department of Earth Science and Environmental Change, University of Illinois Urbana-Champaign, Urbana, IL, 61801, USA.
E-mail address: jdruhan@illinois.edu (J.L. Druhan).

https://doi.org/10.1016/j.gca.2025.01.023
Received 21 July 2024; Accepted 16 January 2025
Available online 25 January 2025

et al., 2013). This relative contribution can be obtained through geochemical mass balance models based on immobile element concentrations (Ferrier et al., 2011) or with end-member mixing models (Capo et al., 1998; Macpherson and Sullivan, 2019). These approaches require the assumption of steady state. For example, Ferrier et al. (2011) used the balance between soil production rates (bedrock weathering + dust incorporation) and denudation rates (physical erosion + chemical weathering), to estimate long-term (10^3 to 10^5 year) dust incorporation rates into soils (Ferrier et al., 2011). Macpherson and Sullivan (2019) used an inverse modeling capacity in the speciation code PHREEQC to attribute the majority of dissolved load in a headwater stream to the dissolution of a reactive dust phase rather than underlying limestone bedrock, suggesting that weathering rates may be greatly overestimated if the contribution of this exogenous source were overlooked.

Aeolian transport of dust can span intercontinental distances (Israelevich et al., 2012; Uno et al., 2009), and presently climate change is intensifying aridification (Cook et al., 2014; Feng and Fu, 2013) and shifting patterns of dust transport (Kim, 2008; Prospero and Lamb, 2003; Salvador et al., 2022) worldwide. The implications of such non-stationarity in mineral-derived nutrient supplies to Critical Zone (CZ) structure and function require extension beyond steady state assumptions to accurately gauge the interactions between dust, weathering, and elemental mass fluxes which are necessary for ecosystem sustainability. Where exogenous supplies are transient, these shifting patterns may propagate into internal bedrock weathering pathways and rates, as well as the resulting chemical weathering fluxes of major elements from the CZ. Process-based reactive transport models (RTMs) of the geochemistry of the near-surface environment hold the potential to describe the coupled interactions of dust deposition, fluid infiltration, bedrock uplift, and internal weathering in a transient framework. To our knowledge, the application of a forward RTM to dust deposition in the CZ has not been demonstrated.

Here, we leverage a new capability (Druhan and Lawrence, 2021) within the open-source multi-component CrunchTope reactive transport software (Druhan et al., 2013; Steefel et al., 2015) to simulate dust deposition and incorporation into an actively uplifting and eroding weathering profile. We do so by adapting the previously developed reactive transport model (RTM) by Golla et al. (2024a,b) for the granitic Sapine watershed in southern France. Their prior model omitted any consideration of solid dust deposition, and their results achieved close agreement with the soil mass-transfer coefficients for the major cations, except for calcium. They suggested that Saharan dust incorporation into the profile could cause the calcium enrichment found in the first meter of soil, leading to a discrepancy between model results and field observations.

The present study achieves three primary objectives. First, we analyze various geochemical data for the Sapine watershed to constrain the elemental composition of dust and the timescales of transport within the weathering profile. Second, we expand and test a new capability within the open-source RTM software that allows solid-phase dust incorporation into an otherwise actively uplifting and eroding weathering profile. Third, we quantify the effects of dust incorporation over the past ~10–15 ka on the internal weathering rates of the watershed. Our novel treatment of dust in an RTM framework allows us to quantitatively constrain the extent of alteration to internal reactivity in the regolith due to the arrival of a new exogenous input source. This capacity improves our ability to consider how shifts in dust deposition influence catchment-scale weathering rates, solute export, and ultimately ecosystem availability of mineral-derived nutrients.

2. Methods

2.1. Site description

Sapine Creek (44° 21′N 3° 48′E) is a headwater stream in Mont-Lozère, in the National Park of Les Cévennes in Southern France (Fig. 1). The catchment is part of the Observatoire Hydrométéorologique Méditerranéen Cévennes-Vivarais (OHM-CV, Boudevillain et al. (2011)), which belongs to the French Network of Critical Zone Observatories (OZCAR) (Gaillardet et al., 2018).

The Sapine basin area is 0.54 km^2 with an altitude that ranges between 1150 and 1450 m above sea level with an average slope of 18° (Martin et al., 2003). The catchment is located 80 km away from the Mediterranean Sea and is subjected to a mountainous Mediterranean climate, with wet, cold winters and dry, warm summers. The mean annual temperature is 7 °C, varying from −5 °C in January to 17 °C in July. Mean annual precipitation is 2000 mm distributed unevenly with most storms occurring in the spring and fall, and mean annual evapotranspiration is 600 mm (Martin et al., 2003). Approximately 80% of the Sapine catchment surface area is covered by a 60-yr old mature beech forest (*Fagus sylvatica*) (Cognard-Plancq et al., 2001; Durand et al., 1991; Lelong et al., 1990). The hydrology and geochemistry of this site are a subject of study since the 1980's, generating rich long-term hydrologic, meteorological, and geochemical datasets (Cognard-Plancq et al., 2001; Didon-Lescot, 1996; Dupraz, 1984; Fernandez et al., 2022; Hanchi, 1994; Kuessner, 2018; Lelong et al., 1990).

The bedrock underlying Mont-Lozère consists of granodiorite rocks with quartz, potassium feldspar, biotite, oligoclase, kaolinite, and illite as the main mineral phases (Kuessner, 2018; Talbot et al., 2004). This granite belongs to the 300-Ma old Pont de Monvert complex (Brichau et al., 2008), which has been intruded by aplite dykes from hydrothermal alteration (Chauvet et al., 2012). Regional uplift rates estimated from Global Positioning System stations are <0.5 mm/yr (Masson et al., 2019), consistent with incision rates measured at ~0.08 mm/yr in the area based on cosmogenic radionuclides (Malcles et al., 2020).

Atmospheric inputs play an important role at Sapine. Using geochemical tracers, Durand et al. (1992) traced the origins of bulk atmospheric depositions in Mont Lozére back to Mediterranean sea salt aerosols, aeolian erosion dust (mainly from the Sahara, Fig. 1), and anthropogenic pollution. Saharan deposition occurs mainly in late spring and is chemically characterized by high calcium (Ca) concentration. Calcium deposition by dust in Les Cévennes was approximately 13.2 kg/ha-yr between 1993 and 1998, based on bulk deposition estimates and meteorological models (Croisé et al., 2005). Forty mineral dust deposition events were recorded between June 1994 and April 2010 in Mont Aigoual, less than 35 km away from Sapine Creek (Lequy et al., 2013). Most recently, the study of Golla et al. (2024b) exemplified the influence of dust deposition on lithium (Li) isotope signatures recorded in the soil and stream of the Sapine catchment.

2.2. Sample collection

A detailed description of the sample collection is provided in Golla et al. (2024b). The Sapine watershed bedrock was characterized from 5 samples collected at multiple locations from large blocks commonly outcropping across the site. These correspond to four samples of porphyritic granite and one aplite, the latter of which is not an abundant rock type in this field site. A regolith core was collected during the installation in 2014 of piezometer P5 at the study site. P5 is located close to the gauging station and solids were subdivided into 20 cm intervals up to a depth of 80 cm. The regolith core collected from P5 is composed of a gradient trending from shallow soils towards chemically weathered bedrock with increasing depth. The top 15 to 30 cm is dark, fine-grained, and homogeneous, while the regolith below this layer is sandier (Kuessner, 2018). Soil samples were dry-sieved using mesh sizes of 63 μm, 250 μm and 2000 μm. The grain size distribution is relatively homogeneous, dominated by the 250–2000 μm fraction at all depths, followed by the >2000 μm fraction. Four plant litter samples and one composite beech leaf sample were collected on October 15, 2024.

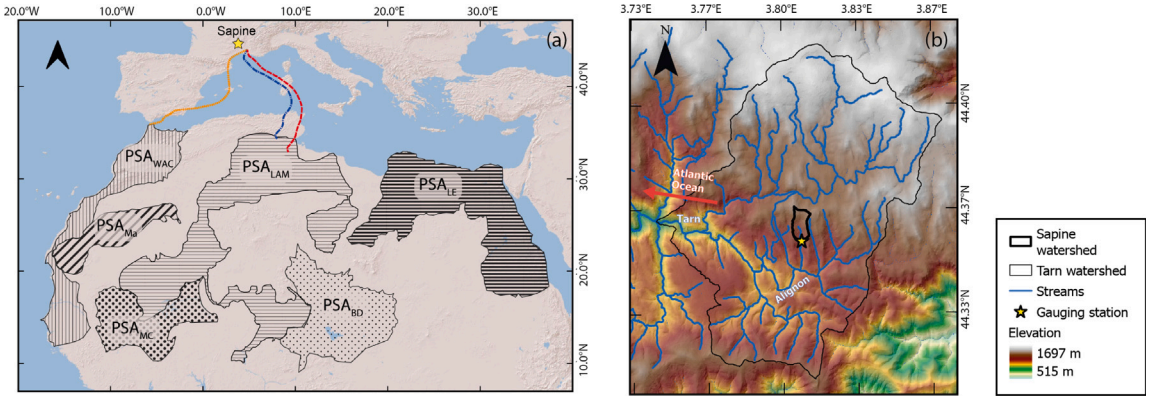

Fig. 1. (a) Map of the Mediterranean region contextualizing the Sapine watershed (44° 21′N 3° 48′E), Mont Lozère, southern France, relative to the Sahara Desert. Green dotted, blue dash dotted, and red dashed lines display 72 h of backward wind trajectories at 30, 500, and 3000 m altitudes respectively, ending on January 2, 1998, 00 UTC, originating from different regions in the Sahara Desert. Trajectories were obtained from the National Oceanic and Atmospheric Administration (NOAA) HYbrid Single Particle Lagrangian Integrated Trajectory (HYSPLIT) model, replicating the trajectories for the city of Avignon (approximately 90 km away from Sapine) presented in Celle-Jeanton et al. (2009). Potential Source Areas (PSAs) of dust are indicated: West African Coast (PSA_{WAC}), Mauritania (PSA_{Ma}), Lybia-Algeria-Mali (PSA_{LAM}), Mali Center (PSA_{MC}), Bodélé Depression (PSA_{BD}), Lybia-Egypt (PSA_{LE}), based on (Guinoiseau et al., 2022) (b) Map of the elevation (color scale) and larger Upper Tarn river watershed boundary (light black line) surrounding the smaller Sapine sub-watershed boundary (dark black line). A yellow star indicates the location of the Sapine creek gauging station. The Digital Elevation Model used for this map was obtained from the Institut Géographique National of France.

Thirty-four rain samples and 206 stream water samples were collected at monthly intervals, and at quasi-hourly frequency during storm events from 2013 to 2019. From 2022 to the present, an additional 7 rain samples and 32 stream samples were collected following the same sampling scheme. Stream water samples are instantaneous records of stream chemistry, while rain samples represent approximately 1-month aggregates. Samples were filtered soon after collection using 0.22-µm cellulose acetate or poly-ether sulfone membranes. Water samples were acidified with purified 16 M HNO_3 to pH 2 and stored in polyethylene bottles that were previously acid-washed. Samples were preserved at 4 °C until further chemical analyses.

2.3. Geochemical analyses

Sample preparation and laboratory analysis were conducted using the Plateforme d'analyse haute résolution (PARI) of the Institut de physique du globe de Paris (IPGP, France). Solid phase rock and soil samples as well as solid reference materials were crushed and milled to a grain size finer than 63 µm using a ball mill, and digested in Teflon vessels using a HF-HNO_3 mixture followed by aqua reggia and HCl refluxing at temperatures higher than 120 °C (Golla et al., 2024c; Kuessner, 2018).

Stream and rainwater major dissolved cations (Na^+, K^+, Mg^{2+}, and Ca^{2+}) and anion (Cl^-, SO_4^{2-}, NO_3^-, and HCO_3) concentrations were determined by ion chromatography using HPLC (Dionex 300 and 120, respectively), with precision equal to or better than 5%. SiO_2 concentrations were obtained using UV–VIS spectrophotometry. The elemental composition of solid samples was measured by quadrupole ICP-MS (Agilent 7900). The external standards materials used for solid samples were GS-N (Vosges granite; Centre de Recherches Pétrographiques et Géochimiques), JB-2 (Oshima volcano basalt; Geological Survey of Japan), BHVO-2 (Hawaiian basalt; United States Geological Survey), and NIST2709a (San Joaquín soil, National Institute of Standards and Technology). Repeated measurements of these solid reference materials yielded an accuracy of ≤3%. The river water reference materials SLRS-5 or SLRS-6 (Saint Lawrence River water, National Research Council of Canada) were repeatedly measured to determine the accuracy of fluid sample characterization, yielding an accuracy of ≤2% for major elements and ≤4% for trace elements (Yeghicheyan et al., 2013, 2019).

2.4. Calculation of mass-transfer coefficients

Non-dimensional mass-transfer coefficients were calculated to describe the relative loss or gain of elements in the regolith relative to bedrock (Brimhall and Dietrich, 1987). For a mobile element j, assuming that an immobile element of reference i is not added to the system from an external source, mass transfer coefficient $\tau_{j,s}$ is defined as

$$\tau_{j,s} = \frac{C_{j,s}C_{i,r}}{C_{j,r}C_{i,s}} - 1 \quad (1)$$

where s is the weathered material (soil or regolith), r is the bedrock (parent material), and C is the concentration [MM^{-1}]. A $\tau_{X/Ti} = 0$ indicates no net gain or loss of element X with respect to the bedrock X/Ti ratio; positive $\tau_{X/Ti}$ values represent enrichment, and negative $\tau_{X/Ti}$ values correspond to depletion. We use titanium (Ti) as our immobile element of reference i (Golla et al., 2024b).

2.5. Strontium and neodymium isotope measurements

Rock, soil, and plant litter samples were analyzed for strontium (Sr) and neodymium (Nd) isotopes. Strontium was separated using the Sr-SPEC resin (Eichrom) following the method developed by Pin and Bassin (1992). Strontium $^{87}Sr/^{86}Sr$ ratios were measured by multi-collector (MC) ICP-MS (Neptune, Thermo-Fischer Scientific). Instrumental mass discrimination was corrected using the natural ratio $^{86}Sr/^{88}Sr = 0.1194$ with an exponential law, and Kr isobaric interferences were removed by blank subtraction (Hajj et al., 2017). An external reproducibility of ±0.00005 (1SD) for the $^{87}Sr/^{86}Sr$ ratio of a pure Sr SRM987 (Sr carbonate, National Institute of Standards and Technology) solution with Sr concentrations between 10 and 100 ng/g was achieved with $^{87}Sr/^{86}Sr = 0.71033$ (n = 31).

Ion-exchange chromatography was used to separate Nd isotopes from the matrix with a two-step separation with TRU-SPEC and Ln-SPEC resins, following the procedure described by Caro et al. (2006). Neodymium $^{143}Nd/^{144}Nd$ ratios were measured by MC ICP-MS (Neptune, Thermo-Fischer Scientific). Instrumental mass discrimination was corrected using the natural ratio $^{146}Nd/^{144}Nd = 0.72190$, applying an exponential law, while the interference of Nd with ^{144}Sm was corrected using the ^{147}Sm signal and natural Sm isotope ratios. Measurement accuracy was checked by recurrently measuring the standard NIST

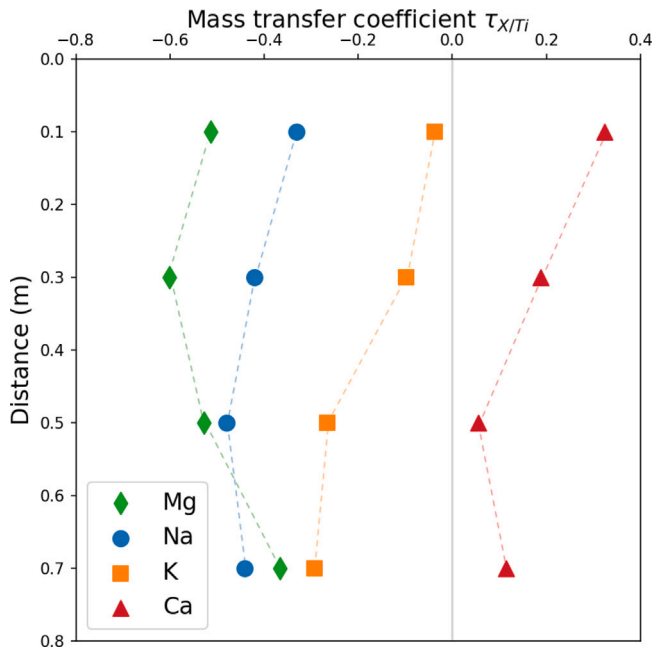

Fig. 2. Mass transfer coefficients ($\tau_{X/Ti}$-values) of Mg (green diamonds), Na (blue circles), K (orange squares), and Ca (red triangles) in the soil relative to the immobile element Ti at depth ranges of 0–20 cm, 20–40 cm, 40–60 cm, and 60–80 cm from the surface in the P5 regolith profile at Sapine. Average depths across each interval (10, 30, 50 and 70 cm from the top core) are used to plot the data.

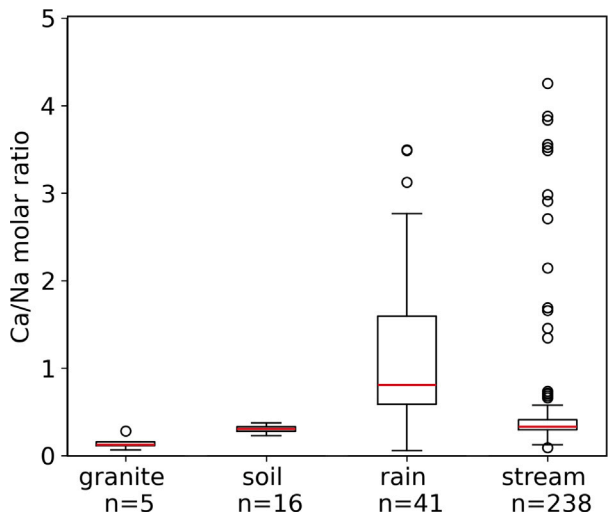

Fig. 3. Box-and-whisker plots of Ca/Na molar ratios for granite, soil, rain, and stream water samples at Sapine, with corresponding number of samples (n). The red line indicates the median, bounded by the box edges indicating the first (Q1: 25th percentile) and third (Q3: 75th percentile) percentiles setting the interquartile range (IQR). The whiskers indicate the minimum and maximum values computed as Q1 −1.5·IQR and Q3 + 1.5 ·IQR. Values above or below the whiskers are considered outliers, assuming that the Ca/Na molar ratios follow a Gaussian distribution.

3135. The external reproducibility of the standard was determined to be 0.16ϵ (2SD, n = 12) for 30 ppb Nd solutions and 0.5ϵ (n = 7) for 15 ppb Nd solutions.

3. Results

The data illustrated here are reported in Golla et al. (2024c) (rock, soil, and water samples) and in the supplement to this present study (Table S1: vegetation samples).

3.1. Mass-transfer coefficients

Dimensionless mass-transfer coefficients (Eq. (1)) illustrate the net loss or accumulation of mass at each depth for the major base cations (Na, K, Mg, Ca) considering the granite bedrock underlying the field site as the only parent material (Fig. 2). Major elements Mg, Na, and K are all depleted relative to bedrock across all depth intervals. Mean τ values and standard deviations across these depths are −0.50 ± 0.10 for Mg, −0.42 ± 0.06 for Na, and −0.17 ± 0.12 for K. In comparison, Ca is enriched across all depth intervals relative to the bedrock, with a mean and standard deviation of +0.17 ± 0.12. All elements at 10 cm depth have higher τ values than at 30 cm depth, reaching $\tau_{Mg/Ti,max}$ = −0.51, $\tau_{Na/Ti,max}$ = −0.33, $\tau_{K/Ti,max}$ = −0.04 and $\tau_{Ca/Ti,max}$ = +0.32. Such enrichment in the very shallowest soil layers has been observed in other beech-covered, nutrient-poor bedrock sites (Berger et al., 2006, 2009). However, unlike Mg, Na and K, Ca enrichment is evident at all depths despite development from a Ca-poor bedrock.

3.2. Ca enrichment across critical zone pools

Calcium-to-sodium molar ratios in bedrock, soil, rain, and stream water samples across the Sapine watershed vary widely (Fig. 3). Our porphyritic granite samples have a Ca/Na ratio of 0.15 ± 0.08, while the single sample of aplite has an even lower Ca/Na ratio of 0.047 ± 0.003. As a point of comparison, the average Ca/Na of porphyritic textured granite in the GEOROC database is 0.32 (n = 707) (GEOROC database (https://georoc.eu/) accessed on March 7, 2024; DIGIS Team, 2023; Lehnert et al., 2000), highlighting the Ca-poor nature of the local bedrock underlying Sapine.

Soils collected between 10 and 70 cm depth show a higher average Ca/Na value than local bedrock (0.30 ± 0.04; Fig. 3) both in terms of bulk composition and for different grain sizes. Rain samples generally have even higher and more variable values than the solids, with an average Ca/Na molar ratio of 1.6 and a median of 0.81. A typical ± standard deviation is not reported for these values due to the strongly skewed nature of the distribution, including four outliers, which are identified as values falling above the sum of the 75th percentile and 1.5 times the interquartile range (Q3 + 1.5IQR). Stream water samples yield lower average and median values (0.49 and 0.33, respectively) than rain, but are also highly variable. In particular, 14 stream data points show Ca/Na molar ratios above 1.0, and 19 are above the Q3 + 1.5IQR criteria for outliers. Mean Ca/Na ratios in both precipitation and stream water samples are strongly skewed by these high values, falling far above the solid phase ratios as well as typical ratios for precipitation derived from marine sources (0.02) (Lyman and Fleming, 1940; Riley and Tongudai, 1967).

This observed Ca enrichment in precipitation and stream water relative to bedrock and soil samples cannot be explained by common pathways of biogeochemical cycling following bedrock dissolution. Ca is commonly incorporated into both secondary phases such as pedogenic carbonates, and vegetative biomass due to nutrient cycling. In contrast, Na is generally considered conservative, leading to an expectation of lower Ca/Na ratios in stream water relative to bedrock (Bailey et al., 2003). Yet here Ca/Na molar ratios are enriched in precipitation and stream water relative to local bedrock and soil samples.

3.3. Sr and Nd isotopes

Isotope ratios of Sr and Nd for the porphyritic granite, soil samples across a range of depths, stream water, and plant litter at Sapine show a clear trend across a mixing diagram (Fig. 4). Granite bedrock samples (n = 4) have the highest $^{87}Sr/^{86}Sr$ and $^{143}Nd/^{144}Nd$ isotope ratios, averaging 0.721 ± 0.001 and 0.51222 ± 0.00002, respectively. Both isotope ratios decrease from the deepest sample ($^{87}Sr/^{86}Sr$ = 0.718

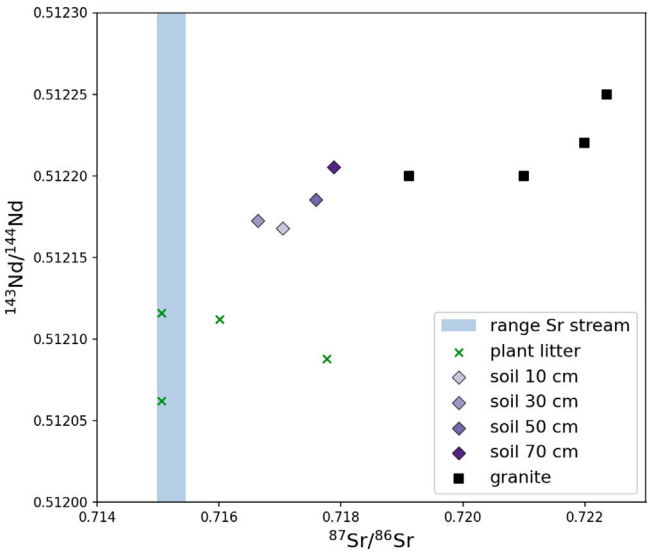

Fig. 4. Mixing diagram of $^{87}Sr/^{86}Sr$ vs. $^{143}Nd/^{144}Nd$ for stream water, plant litter, soil, and porphyritic granite bedrock samples.

and $^{143}Nd/^{144}Nd$ = 0.512205) to the shallowest ($^{87}Sr/^{86}Sr$ = 0.717 and $^{143}Nd/^{144}Nd$ = 0.512168). These values are the weighted average across a range of grain size fractions (< 63 μm, 63-250 μm, 250-2000 μm and > 2000 μm) at each depth (Golla et al., 2024c). Plant litter samples yield an average value of $^{87}Sr/^{86}Sr$ = 0.715974 and $^{143}Nd/^{144}Nd$ = 0.512095 (n = 4). The low solubility of Nd prohibited measurements in our water samples, but stream Sr ratios are $^{87}Sr/^{86}Sr$ = 0.7152 ± 0.0002 (blue vertical band).

4. Discussion

4.1. Field evidence of dust deposition

Mass-transfer coefficients (Section 3.1), Ca/Na molar ratios (Section 3.2), and Sr and Nd isotopes (Section 3.3) all show clear evidence that an exogenous mass source affects the Sapine watershed. This is consistent with a recent study of lithium (Li) dynamics at Sapine by Golla et al. (2024b), where explicit treatment of an atmospherically derived Li input source was required to accurately model the distribution of Li and its isotope ratios through the watershed. They estimated ~96% of Li was atmospherically derived and of Saharan origin based on Li/Na ratios. Similarly, enrichment in Ca through the upper layers of the soil profile (Fig. 2) cannot be explained without an additional input source. This inference is underscored by disagreement between field observations and model results of Ca content in the soil profile reported in Golla et al. (2024b). Their multi-component RTM for the site, which describes the principal water-rock reactions producing this weathering profile, was not able to reproduce observed τ_{Ca} values, instead predicting that in the absence of an exogenous atmospheric Ca input, the topsoil τ_{Ca} would be −0.46. Our observed enrichment to positive $\tau_{Ca/Ti}$ values across the upper 80 cm of the weathering profile contradicts this RTM simulation. Similar results were obtained when calculating mass-transfer coefficients using niobium (Nb) and zirconium (Zr) as the immobile element in Eq. (1).

To some extent, enriched Ca/Na ratios in the shallowest layers of a weathering profile may be produced through ecosystem recycling (Berger et al., 2006). Calcium is commonly required by vegetation as a macronutrient (White and Broadley, 2003) and incorporation of organics into the weathering profile can enrich Ca relative to a less essential element like Na. Such biologically-driven enrichment is supported by the Ca/Na molar ratios of plant litter samples collected at the site, which range between 34 and 53 (Kuessner, 2018). However, this ecosystem has developed on a naturally Ca-poor granite, and hence in the absence of exogenous inputs, this enrichment would require a corresponding Ca-depleted pool which we find no evidence for. Instead, soils and stream water are also Ca-enriched compared to bedrock (Fig. 3). Furthermore, Sr and Nd isotopes independently point to an exogenous mass input, where the decrease of both $^{87}Sr/^{86}Sr$ and $^{143}Nd/^{144}Nd$ isotope ratios in soil and plant litter samples compared to the granitic bedrock can only be the result of mixing with another mass source with lower isotope ratios. Thus, exogenous atmospheric source(s) rich in Ca must be considered in this site.

We hypothesize that atmospheric deposition of Ca-rich dust of Saharan origin is affecting the Sapine watershed. This is based on both the field measurements presented here (Sections 3.1, 3.2 and 3.3) and previous studies indicating widespread deposition of Saharan dust across the western Mediterranean region (Celle-Jeanton et al., 2009; Durand et al., 1992; Lequy et al., 2013; Loye-Pilot and Morelli, 1988; Vincent et al., 2016). The mineralogy of Saharan dust can be variable (Formenti et al., 2011; Guinoiseau et al., 2022). Samples collected during a dust event in Southern Spain had carbonate contents ranging between 12%–24% (Rodriguez-Navarro et al., 2018). Even with carbonate contents much lower than this, an exogenous dust input could easily create a highly Ca-enriched input relative to the local bedrock underlying Sapine.

4.2. Contribution of an exogenous source to soils and stream based on mixing models

The fraction of dust contributing to the soil profile can be constrained by mass balance based on Nd concentrations and isotope ratios. Strontium is not used for this purpose because of the variability in Sr concentrations and isotope ratios between rock-forming minerals and the capacity for these minerals to dissolve at different rates, potentially leading to vertical variation in Sr isotope ratios of the weathered regolith. Using our granite samples as the bedrock end member ($[Nd]_r$ = 36.3 ppm and $(^{143}Nd/^{144}Nd)_r$ = 0.51222) and the average of 13 samples from the Lybia - Algeria - Mali region ($[Nd]_d$ = 58 ppm and $(^{143}Nd/^{144}Nd)_d$ = 0.51200) (Guinoiseau et al., 2022) as the dust end-member, we estimate that the fraction of soil mass attributed to dust at Sapine is highest in the shallowest sample ($f_{soil}^{total\ dust}$ = 0.17 at 10 cm depth) and decreases with depth to $f_{soil}^{total\ dust}$ = 0.04 at 70 cm.

The fraction of Ca in the stream specifically derived from dust can be quantified in a similar way using a binary mixing equation based on the Na/Ca ratios of bedrock and of the carbonate fraction of dust. This approach assumes that ecosystem cycling is at steady state and does not present an additional source or sink of Ca in the system, and further that the main Ca-bearing phase in the dust end-member is a carbonate with Na/Ca ratio of zero. The median Na/Ca ratio of Sapine stream water samples is 3.03 and the average granite ratio is 6.67, leading to a fraction of Ca contributed from carbonate dust of 0.55. A wide range of Ca/Na ratios surround this median value (Fig. 3), underscoring the episodic nature of dust contributions to the system. As a point of comparison, Golla et al. (2024b) used a similar approach to estimate that 96% of Li in precipitation at the site was derived from Saharan dust. These authors showed that a simple correction for atmospheric Li inputs to the Sapine stream would yield values over 100%, clearly indicating that the watershed is assimilating and internally processing this dust input through (bio)geochemical pathways rather than simply mixing exogenous and local contributions to stream chemistry. In what follows we advance our analysis of the effects of this exogenous input on the reactivity and elemental fluxes within and through the system using a reactive transport framework.

4.3. Dust deposition in an RTM framework: Proof of concept

Here we employ a new capability in the multi-component reactive transport code CrunchTope (Druhan and Lawrence, 2021) that allows

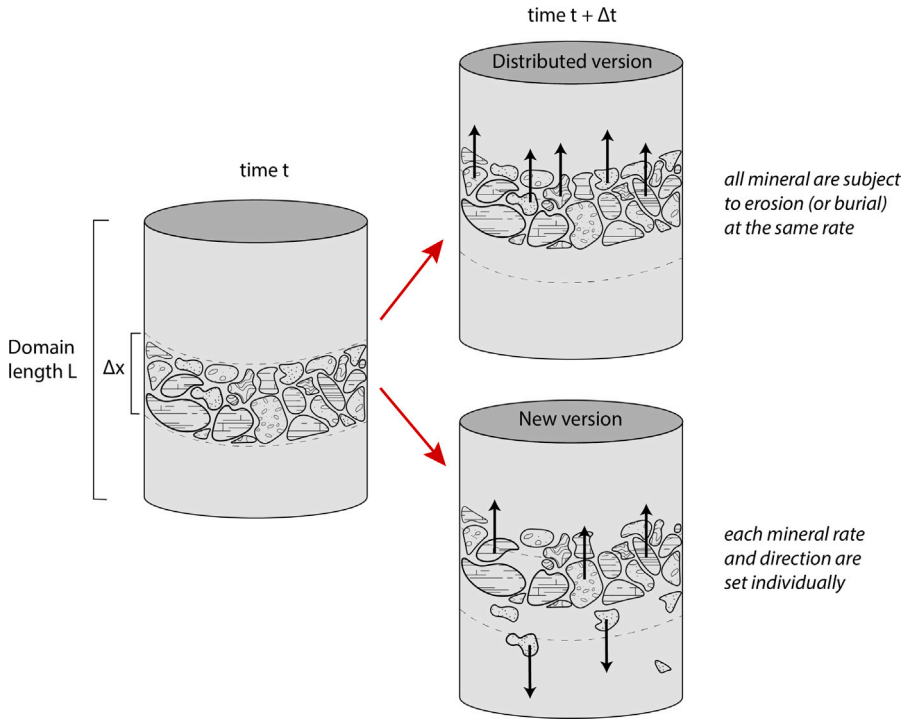

Fig. 5. Sketch illustrating the collective mineral movement in the distributed CrunchTope version, where all minerals move in the same direction and magnitude; and the individual movement allocation of minerals newly implemented in the present work, where each mineral can move in a user-specified direction at its own linear velocity. Minerals moving upwards are subject to erosion when they reach the top boundary of the domain, whereas minerals traveling downwards exit the base of the domain.

for explicit simulation of solid phase dust deposition to the surface of an actively uplifting and eroding weathering profile. This alleviates the need to assume an instantaneous balance between the total rate of mass addition and regolith denudation underlying previous models for dust incorporation (Section 1). Here, we offer a means of quantifying the effects of dust deposition, transport, and dissolution on the chemical weathering rates of open systems in a transient framework.

In the distributed version of CrunchTope (Druhan et al., 2013; Steefel et al., 2015), all minerals in the profile move up or down at the same constant linear velocity in the same direction, either entering the domain from the bottom and eroding at the top (uplift) or entering the domain from the top and exiting at the bottom (burial). For the present work, changes in the source code were necessary to decouple this collective mineral transport following the approach of Druhan and Lawrence (2021). In this new implementation, each mineral's transport direction and velocity are assigned individually (Fig. 5). Updates necessary to the software are detailed in Druhan and Lawrence (2021), here, we adapt their soil organic carbon model to a generic mineral weathering profile subject to an exogenous dust input. Classically, all mineral phases composing bedrock enter the base of the domain and move upward at a rate appropriately representing uplift. These solids are evolved through the profile as a result of chemical weathering, ultimately leading to erosion off the top of the domain of a solid phase composition more appropriately representing soil (e.g., Golla et al. (2024b)). Using the Druhan and Lawrence (2021) implementation, we add a set of new mineral phase(s) to the top of the domain which move downward at a unique velocity appropriately representing a dust deposition and burial rate.

Here we develop and validate appropriate behavior of this new model in a sequence of two simulations. First, we offer a proof-of-concept model in which dust is applied to a generic inert bedrock. This example is employed as a verification that the new solid phases are appropriately supplied and transported from the top down through the domain as the preexisting bedrock continues to uplift and erode. Mass balance of all components across all phases is tracked through time and we confirm that a new steady state is established. Second, we apply a novel solid phase dust input to the top of the domain of the RTM for the Sapine watershed previously developed by Golla et al. (2024b).

Table 1
Parameterization of the proof-of-concept (PoC) and Sapine watershed CrunchTope models allowing for differential solid-phase transport.

Parameter	PoC	Sapine
Domain size L [m]	5	20
Grid discretization [m]	0.01	0.01
Temperature [°C]	25.0	7.0
Initial bedrock porosity ϕ [–]	0.1	0.1
Bedrock uplift and erosion rate v_r [m/yr]	10^{-4}	10^{-4}
Darcy flux q [m^3 water/m^2 porous media-yr]	1.4	1.4
Dust burial rate v_d [m/yr]	3.7×10^{-5}	3.7×10^{-5}

The proof-of-concept model consists of a one-dimensional, $L = 5$-m long domain that represents a vertical profile made up of a generic, non-reactive "bedrock" mineral (Table 1). The domain is discretized to 500 grid cells of 0.01 m each. Solid phase uplifts from the bottom and erodes at the top at a steady rate v_r of 10^{-4} m/yr. We apply a constant infiltration rate to the top boundary which drains downwards through the porous media, and discharges at the bottom boundary, at a constant velocity q of 1.4 m/yr. These values are arbitrary, but loosely based on the parameterization employed by Golla et al. (2024b) for the Sapine watershed. Dust deposition is initiated by introducing a new generic mineral phase termed "dust" as an upper boundary condition with a burial rate v_d of 3.7×10^{-5} m/yr to the top of the domain (Table 2). To differentiate between bedrock and dust material, we assign the former the composition of quartz (SiO_2) and the latter the composition of calcite ($CaCO_3$), though we emphasize that, for this proof-of-concept simulation, the capacity for these two "minerals" to react is entirely controlled by our choice of reaction parameters and not based on literature-reported values for quartz or calcite. We run two scenarios with this simplified setup: scenario (1) in which dust is unreactive, to test the differential movement of minerals; and scenario (2) in which dust is allowed to dissolve. Scenario 2 is subdivided into

Table 2
Mineral volume fractions, mineral surface areas, and kinetic rate constants used in the proof-of-concept (PoC) and Sapine watershed models. Solid phase initial conditions of the POC model are Bedrock. Solid phase boundary conditions include a supply of Bedrock uplifting from the base of the domain and a supply of Dust depositing onto the top of the domain. Mineral rates in the PoC simulations are arbitrarily set and not based on any literature values for quartz or calcite. Rather, the choice of a rate constant 10^{-45} mol/m^2-s is so low as to render the phase effectively inert, while in scenario 2a the $10^{-6.5}$ mol/m^2-s value allows the "dust" phase to dissolve partially and in 2b the $10^{-5.0}$ mol/m^2-s value enables total dissolution within the profile. Infiltrating water contains 1×10^{-5} mM Ca^{2+} and SiO_2 at a pH of 5.5 in equilibrium with 0.01 bar CO_2. In the Sapine granite weathering model, mineral phase parameter values marked with * come from (Golla et al., 2024b), while calcite and nonreactive dust values are new implementations in this study. The initial condition of our Sapine model is the final steady state result of Golla et al. (2024b). Solid phase boundary conditions include supply of the minerals marked with * at the base of the domain through uplift and supply of calcite and nonreactive dust as deposition at the top of the domain. The full stoichiometry of these mineral weathering reactions is given in Golla et al. (2024b).

Condition	Mineral formula	Initial volume fraction [m^3/m^3]	Mineral surface area [m^2/g]	log K [mole/m^2-s]
PoC model				
Bedrock	SiO_2	0.90	1.9×10^{-5}	−45.0
Dust	$CaCO_3$	0.05	10	−45.0 *(Scenario 1)* −6.5 *(Scenario 2a)* −5.0 *(Scenario 2b)*
Sapine granite weathering model				
Quartz*	SiO_2	0.30	1.9×10^{-5}	−13.99
K-Felsdpar*	$KAlSi_3O_8$	0.23	2.9×10^{-4}	−12.41
Oligoclase*	$Na_{0.9}Ca_{0.1}Al_{1.1}Si_{2.9}O_8$	0.29	4.1×10^{-4}	−11.84
Biotite*	$KMg_2FeAlSi_3O_{10}(OH)_2$	0.08	1.1×10^{-4}	−12.55
Kaolinite*	$Al_2Si_2O_5(OH)_4$	0.0001	10	−13.18
Calcite	$CaCO_3$	10^{-30}	1	−45.00 *(profile)*
		0.0075	1	−5.00 *(dust boundary)*
Nonreactive dust	$Al_2Si_2O_5(OH)_4$	10^{-30}	10	−45.00 *(profile)*
		0.15	10	−45.00 *(dust boundary)*

two cases (a) in which the reactivity of the dust mineral is set to a value leading to its partial dissolution as it transits the domain and (b) in which this reactivity is enhanced, leading to full dissolution before the dust mineral reaches the bottom boundary. The reactivity of this dust solid phase is regulated by a user-defined rate constant (Table 2), and subject to the saturation state of the fluid phase with respect to this mineral.

Erosion rates are commonly higher than dust deposition rates (Mahowald et al., 2005; Schaller and Ehlers, 2022), and yet exogenous solids are incorporated into soils across a variety of landscapes due to mixing mechanisms like infiltration and bioturbation (Derry and Chadwick, 2007; Kaste et al., 2007; Yoo et al., 2011). In our modeling approach, we take a simplified representation of this behavior by assigning uplift to bedrock-derived minerals and burial to dust-derived minerals contemporaneously. This essentially makes the exogenous solids immune to erosion, allowing them to transit downward at a rate that is slower than the concurrent rate of erosion occurring at the top boundary of the soil profile, as they would in natural systems under the effect of bioturbation and transport through porosity. This means that in our approach the rate of dust incorporation to the weathering profile can be considered as a net flux.

Current understanding of the transport processes underlying dust addition to weathering profiles is incomplete; however, for the purpose of the present study we offer a simplified representation of (1) incorporation of solids deposited on the land surface into deeper horizons through mixing processes such as bioturbation; and (2) advection of fine dust particles through the open pore space in association with infiltration and drainage of meteoric water. In the present study, a constant dust deposition rate (v_d) is implemented using the same first-order upwind numerical scheme as earlier applications of uniform solid phase burial, *e.g.,* marine diagenesis (Fantle et al., 2010; Huber et al., 2017) and uplift (Golla et al., 2024b; Guinoiseau et al., 2021). Until now, this simple implementation has never been tasked with representing a solid phase tracer breakthrough curve released at the top of the domain and propagating to the base. A substantial degree of numerical dispersion is associated with such a low-order scheme applied at the timescales of solid phase transport (10^3 to 10^4 years). We use this behavior to represent the diffusion of exogenous input within the bedrock-derived mineralogy, and further analyze the magnitude of this diffusion in application to the Sapine model in Section 4.4 and Supplementary Data. A significant, yet subordinate role of diffusion compared to advection in the downward transport of dust is consistent with Gray et al. (2020), who used a combination of field observations and modeling to constrain vertical transport Péclet numbers ranging between 0.1 and 1.0 for well-developed soils affected by bioturbation and plant roots.

Appropriate behavior of the new model implementation is confirmed by tracking the mass of Ca distributed across all phases and verifying that mass balance between inputs to and outputs from the model domain is first perturbed and then reestablished following the initiation of dust deposition. The Ca flux [moles/m^2 porous media-yr] through the solid phase is given as:

$$J_{Ca,solid} = \frac{\phi_m}{V_{m,dust}} \cdot \frac{\text{moles Ca}}{\text{mole mineral}} \cdot v_d \quad (2)$$

where ϕ_m is the mineral volume fraction per unit volume of porous media [m^3 mineral/m^3 porous media], $V_{m,dust}$ is the molar volume of the mineral representing dust [m^3 mineral/mole mineral], and v_d is the downwards transport velocity of dust [m/s]. This equation accounts for the fact that dust deposition accumulating on the weathering profile surface can only penetrate into the profile through the fraction of total porous media that is open pore space. At present the model burial rate v_d is constant and unaffected by subsequent evolution of mineral volume fractions (both dust and native rock) due to fluid-mineral interactions. Future model development could allow for coupling between porosity evolution and dust burial flux where sufficient data are available to constrain this linkage. The fluid phase Ca flux [moles/m^2 porous media-yr] is cast into the same units for direct comparison:

$$J_{Ca,fluid} = [Ca^{2+}]_{aq} \cdot \rho_f \cdot q \quad (3)$$

where $[Ca^{2+}]_{aq}$ is the concentration of Ca in water [mole Ca/kgw], ρ_f is the density of the transport fluid [kgw/m^3 water], and q is the downwards transport velocity of water [m^3 water/m^2 porous media-yr]. At present the dust burial rate v_d is assigned independently from the water velocity, though future simulations could be designed to allow coupling between the two parameters. Solute concentrations carried by the infiltrating water at the top of the domain are subtracted from effluent concentrations when calculating $[Ca^{2+}]_{aq}$, yielding a flux

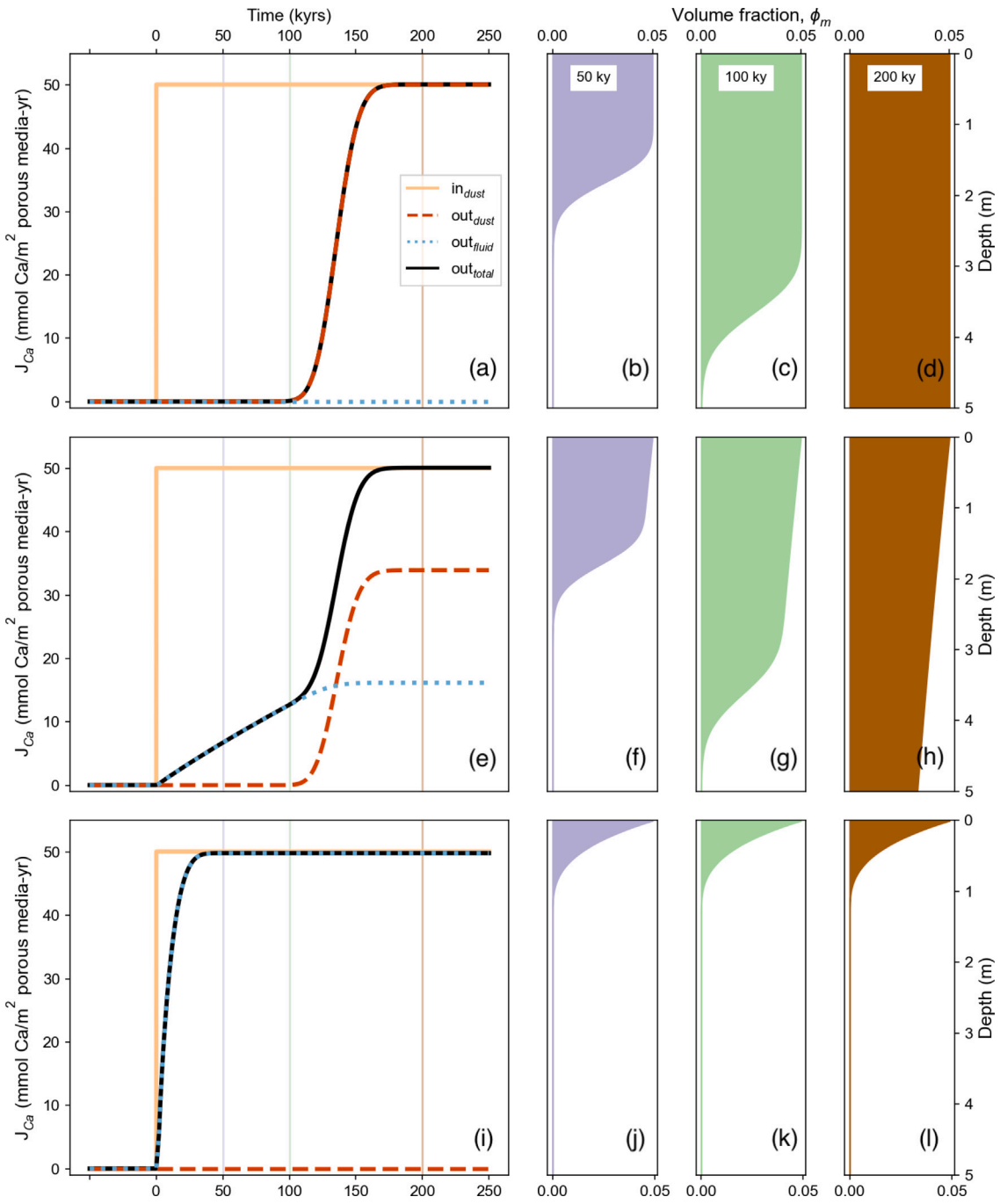

Fig. 6. Evolution of Ca fluxes in the unreactive (scenario 1), partially reactive (scenario 2a), and fully reactive (scenario 2b) cases of the proof-of-concept model and corresponding volume fractions of bedrock and dust over time. At the start of the simulations, there is no Ca present in the fluid or solid phases. Calcium begins to enter the domain as solid-phase dust starting at 0 ky (solid orange line in (a),(e), and (i); and dust volume fractions evolve between 0 and 0.05 in (b)–(d),(f)–(h), and (j)–(l)). In (a) - (d), the dust mineral phase does not dissolve (Table 1), reaching the base of the domain after ~135 ky. In (e)–(h), a fraction of the incoming dust is dissolved, such that both water and solid phases carry Ca at the base of the domain. In (i)–(l), dust fully dissolves within the first meter of the domain, and Ca is fully exported as a solute efflux.

that is entirely based on mass derived from fluid-mineral interactions.

In all scenarios, the initial bedrock is solely composed of SiO_2, such that Ca is essentially absent at the start of the simulation. This inert "bedrock" uplifts and erodes at a uniform rate, while the fluid infiltrates and drains the profile. The entire system is at steady state. Dust deposition begins at the top of the profile at an arbitrary time of 0 ky. In scenario 1 (Fig. 6a–d), this dust is unreactive, such that none of the Ca is dissolved into the fluid phase and the aqueous flux of Ca at the base of the domain is zero. The dust mineral is implemented in the CrunchTope model as a volume fraction of the total porous media, which is assigned to occupy a maximum of 0.05 in all these scenarios (Fig. 6b–d), yielding an incoming solid Ca flux of 50 mmol Ca/m^2 porous medium-yr (Fig. 6a, solid orange line). Calcium is lost as a solid phase through the lower boundary of the domain (Fig. 6a, dashed red line). When the incoming and outgoing Ca fluxes reach a new equivalency (orange and black solid lines), mass balance is reestablished and a new steady state is achieved. In scenario 2a (Fig. 6e–h), dust partially dissolves as it transits the porous medium (Table 2), such that Ca exits the domain through the lower boundary both as a solute (Fig. 6e, blue dotted line) and as the remaining solid (Fig. 6e, red dashed line). This results in a smaller volume fraction of solid phase dust exiting the base of the domain relative to scenario 1.

In the extreme case of highly reactive dust (scenario 2b), the entirety of the exogenous input dissolves during transit through the porous media and it is completely exported as dissolved mass (Fig. 6i–l, blue line).

In scenarios 1 and 2a, the dust does not (fully) dissolve, so steady state is only achieved once the solid-phase dust reaches the bottom boundary. This is determined by the dust transport velocity. In this example, the solid dust transits the 5 m domain in 135 ky. In scenario 2b, a much shorter time is necessary to establish a new steady state because all incoming dust is fully dissolved within the first meter of the domain. In the example illustrated (Fig. 6f) this balance stabilizes within 40 kyrs. Hence the timescale over which a system establishes a new steady state after accommodating a new exogenous input source is strongly dependent on the relative rates of solid phase transport and mineral reactivity, essentially a Damköhler number (Da) in application to a reactive solid phase transiting the system. For a higher Da, dust incorporation does not reach as deep into the profile, and steady state is established faster. As Da decreases, the solid phase reaches further into the domain and the timescale to reach steady state approaches L/v_d.

4.4. Dust deposition in an RTM framework: application to the Sapine catchment

Having verified the appropriate behavior of this differential mineral movement capability in a simplified framework, we now turn to the CrunchTope model for the Sapine watershed developed by Golla et al. (2024b) to constrain the effects of reactive dust deposition on the internal structure and reactivity of the weathering profile. The earlier model was capable of achieving good agreement with field observations for most major base cation soil depletion profiles (Na, K, Mg), but strongly under-predicted $\tau_{Ca/Ti}$. This was based on the assumption that the only parent material for the soil profile is the Ca-poor granitic bedrock, and Golla et al. (2024b) suggested the mismatch was likely due to an exogenous dust input. Here we update the model to include Saharan dust deposition. In doing so we verify whether the inclusion of this exogenous source reconciles modeled and measured $\tau_{Ca/Ti}$, and consider how the introduction of carbonate-bearing dust over the past ~12 kyr has impacted soil chemical composition and mineral weathering rates at the field site.

4.4.1. Model parameterization and recovery of $\tau_{Ca/Ti}$

We use the same mineralogy, mineral rate constants, uplift and erosion rates, and fluid infiltration velocities as Golla et al. (2024b) (Tables 1 and 2). Briefly, their model consists of a 1D domain of length 20 m, representative of a typical water flow path in Sapine, discretized into 2000 cells of 0.01 m. The initial condition was an unweathered granite with a porosity of 10%, and mineral volume fractions corresponding to 30% quartz, 23% K-feldspar, 29% oligoclase, and 8% biotite. The simulations were allowed to evolve over geologic timescales, reaching a new steady state at ~ 200 kyr. At this new stable state, porosity at the top of the domain reaches ~20%, and secondary kaolinite accumulation occupies ~10% of the upper soil porous media.

Our simulations apply dust as a new fixed boundary condition to the top of this domain once the original (Golla et al., 2024b) model has reached steady state. We use a long-term average dust deposition flux $J_{d,solid}$ for the western Mediterranean of 10 g/m^2-yr (Vincent et al., 2016), which we convert into a downward burial rate v_d (Table 1):

$$v_d = \frac{J_{d,solid}}{\phi \cdot \rho_d} \tag{4}$$

Eq. (4) assumes that this exogenous input moves through the available open pore space (ϕ). Together with an assumed density ρ_d = 2.7 g/cm^3, this results in a long-term average dust transport velocity of 3.7×10^{-5} m/yr. This v_d is 2–3 orders of magnitude smaller than values obtained from ^{210}Pb and ^{137}Cs tracer experiments in forested soils. However, it was noted that in forests with reduced earthworm

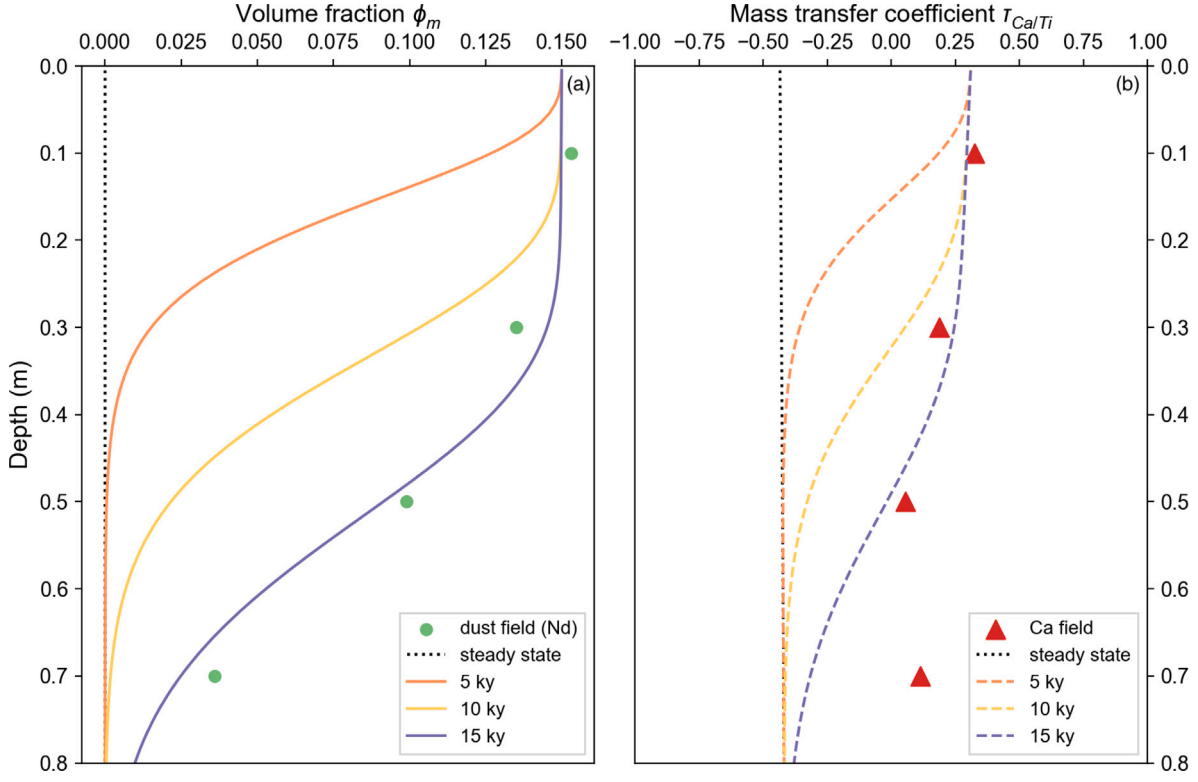

Fig. 7. (a) Mineral volume fraction over the first meter of soil in Sapine Creek. Calculated volume fractions (green points) are based on field observations (Section 4.2). The front of dust minerals (calcite plus unreactive kaolinite) is illustrated over relevant timescales of Saharan dust exports (solid-colored lines). (b) Measured (red triangles) and modeled (dashed lines) mass-transfer coefficients of Ca at 5, 10, and 15 ky after the initiation of dust deposition. The black vertical dotted line indicates the expected τ value for Ca based on soil weathering only (no dust). Analysis of the diffusive behavior evident in these profiles is provided in Supplemental Information Figures S1 and S2.

activity, the mixing velocities could be smaller (Kaste et al., 2007; Yoo et al., 2011). Both cold temperatures and acidic soils characteristic of Sapine could reduce such bioturbation (Li et al., 2002).

The amount of dust applied to the top of the domain was calibrated by converting the Nd isotope mixing model (Section 4.2) into a volume fraction of dust as a function of depth through the upper 80 cm of the soil profile (Fig. 7a). The dust and porous media densities are essentially the same ($\rho_d = \rho_r = 2.7$ g/cm^3) and hence this conversion only requires an adjustment for porosity (ϕ). At 10 cm, this yields a total dust volume fraction (ϕ_m) of 0.15 which is the value we assign in the model at the top boundary condition (Fig. 7a). As the dust-enabled RTM is run forward in time the exogenous solid is transported downward (Eq. (4)), subject to mixing with the native porous media as a result of the numerical dispersion described in Section 4.3. This numerical dispersion can be mitigated through reduction of both the model grid spacing and maximum timestep (Figure S1). However, for the present simulations, progressive smearing of the front of the dust input closely resembles the calculated dust volume fractions over the upper 80 cm measured in our soil profiles after 15 kyr. This is consistent with the timescales of Saharan desert drying and enhancement of dust export towards the end of the African Humid Period, which has spanned the last ~10–15 kyr (Zielhofer et al., 2017). Hence the degree of numerical dispersion produced by our low-order advective scheme for solid phase transport is appropriately representing the extent of physical dispersion observed in our data while simultaneously facilitating reasonable model simulation times. Based on a second moment analysis (Figure S2), this mixing corresponds to a diffusion coefficient of 1.1×10^{-6} m^2/yr. Here we emphasize that no excessive effort was placed on fitting the model to these data, and we take the close agreement between model outputs and data as an indication that the RTM is adequately reproducing the transient propagation of a solid phase exogenous input to this weathering profile over millennial timescales.

We next partition this dust into specific mineral phases based on the constraints described in Sections 3.1 and 4.2. Saharan dust has variable and complex mineralogy depending on the region of provenance, but it is generally composed of carbonates and phyllosilicates (Formenti et al., 2014; Rodriguez-Navarro et al., 2018). Our model represents these two mineral groups as calcite and kaolinite, respectively. The inclusion of dust-derived calcite in the soil could explain both the enrichment in Ca/Na observed in our rain and stream samples (Fig. 3) as well as the isotopic shift in Sr in the topsoil. Similarly, kaolinite could cause the departure in Nd from bedrock isotopic values (Fig. 4). The relative proportions of these two minerals are specified based on a comparison of field and model calcium mass-transfer coefficients (Fig. 7b). An upper boundary porous media volume fraction of 0.75% calcite yields good agreement with observations $\tau_{Ca/Ti}$, and the remaining 14.25% is thus assigned to kaolinite. Again, we make no excessive effort to fit the model to these data, and in this instance, good agreement is preserved over the upper ~60 cm. The deepest measured value (+0.11) is higher than our model results (−0.32), suggesting that there may be additional factors influencing the transmission of the solid phase carbonate (e.g. ecosystem effects, bioturbation or sorption) beyond the simple representation implemented here. Given that kaolinite is already present as a secondary mineral phase in the Golla et al. (2024b) model, we add this dust-associated version of the mineral separately using the same mineral stoichiometry and reactive parameterization (Table 2).

Explicit application of a solid-phase exogenous dust component into the Golla et al. (2024b) Sapine model reconciles prior disparity between the simulation and field observations of Ca accumulation in the soil. Clearly, this is a result of the fact that we assigned the volume fraction of calcite in the dust based on Fig. 7b. However, we did so subject to an independently constrained dust burial rate and total dust volume fraction. The resulting proportion of our dust composed of carbonate vs. phyllosilicate is realistic, and consistent with the range of values reported for Saharan desert composition (Formenti et al., 2014). The exogenous calcite phase occupies only 0.75% of the total topsoil porous media volume, yet simulated $\tau_{Ca/Ti}$ values at the top shift from −0.43 (reported in Golla et al. (2024b); Fig. 7b, dotted black line) to +0.31 in our new model. After 15 kyr the simulated $\tau_{Ca/Ti}$ profile (Fig. 7b) looks quite similar to the bulk dust volume fraction profile (Fig. 7a), but we note that the calcite is reactive and subject to dissolution at much faster rates than the kaolinite. This behavior is considered further below.

4.4.2. Effects of dust input on the sapine weathering profile

When an exogenous solid phase enters the top of the domain, it becomes a new parent material to the soil (Lawrence et al., 2013). However, the relative effects of this input are element-specific. When we expose the prior Sapine model (Golla et al., 2024b) to dust deposition the system is pushed out of steady state, but this is much more noticeable in the Ca fluxes than in the other elements composing the silicate mineralogy. The solid Ca flux entering the system as dust (Fig. 8a) represents 21% of the total solid Ca influx; while the remaining 79% is provided by the uplift of oligoclase into the base of the domain (Fig. 8b). As soon as calcite enters the system, Ca fluid efflux starts increasing, due to the higher reactivity of this mineral compared to oligoclase (Table 2). Over the 15 kyr simulation, Ca fluid efflux exiting the system increases by 7.5% since the start of dust deposition. As a point of comparison, the incorporation of kaolinite at the top of the domain due to dust deposition only minimally affects the SiO_2 mass balance as it represents only 3.6% of the total incoming Si to the system. The result is a lack of discernible increase in SiO_2 fluid efflux (Fig. 8c) over the same time interval.

Dust incorporation and dissolution allow for the concurrent enrichment of soil $\tau_{Ca/Ti}$ values and high Ca/Na molar ratios in the stream water (Fig. 3). It also suggests that observed Ca enrichment in the profile while the other base cations are exported (Fig. 2) is not principally an effect of nutrient retention by the ecosystem. For dust-impacted field sites such as Sapine, Lawrence et al. (2013) proposed an alternative mass transfer coefficient considering both local bedrock and exogenous dust as parent materials through a weighted average of the two source end-member chemical compositions. In the Sapine soil, the average mass fraction contributed by dust in the first 80 cm of soil, according to Nd isotopes (Section 4.2), is 12% ($f_{soil}^{totaldust}$ at 10 cm = 0.17; at 30 cm = 0.15; at 50 cm = 0.11; and at 70 cm = 0.04), and therefore the contribution from the bedrock is the remaining 88%, assuming no other end-members apart from dust and bedrock. Thus, applying the approach from Lawrence et al. (2013) with a parent material composed of 88% Sapine granitic bedrock and 12% dust, our updated $\tau_{Ca/Ti}$ values become −0.21, −0.38, −0.39, and −0.38 at depths of 10, 30, 50, and 70 cm, respectively. This is much more consistent with the other base cations (Fig. 2).

What uniquely distinguishes our RTM approach from these prior steady-state models is the ability to develop the system through time considering reactive transport processes from the initiation of an exogenous input. Dust deposition events are ongoing at Sapine, and our RTM approach can be used to predict system behavior at a point when a new steady state is reached. The time required to reach this point is element-specific and subject to the novel framing of a Damköhler number described in the proof-of-concept model (Section 4.3). If we allow our model to run for timescales beyond the those over which Saharan dust deposition has prevailed (~ 15 kyr), keeping all other parameters constant, Ca reaches a new steady state 200 ky after dust deposition onset. This is controlled by the calcite reaction rate, which leads to total calcite dissolution by a depth of 13 m, similar to the proof-of-concept model scenario 2b (Fig. 6i–l). For Si, a new steady state is reached 540 ky after dust deposition onset, because the silicate mineral component of the dust is much less reactive. This is similar to the proof-of-concept model scenarios 1 and 2a (Fig. 6a–h), such that the timescale is determined by the ratio L/v_d.

Using the RTM we may further consider the extent to which, over these timescales, adding a carbonate mineral should neutralize the reactive potential of infiltrating precipitation, leading to shifts in the

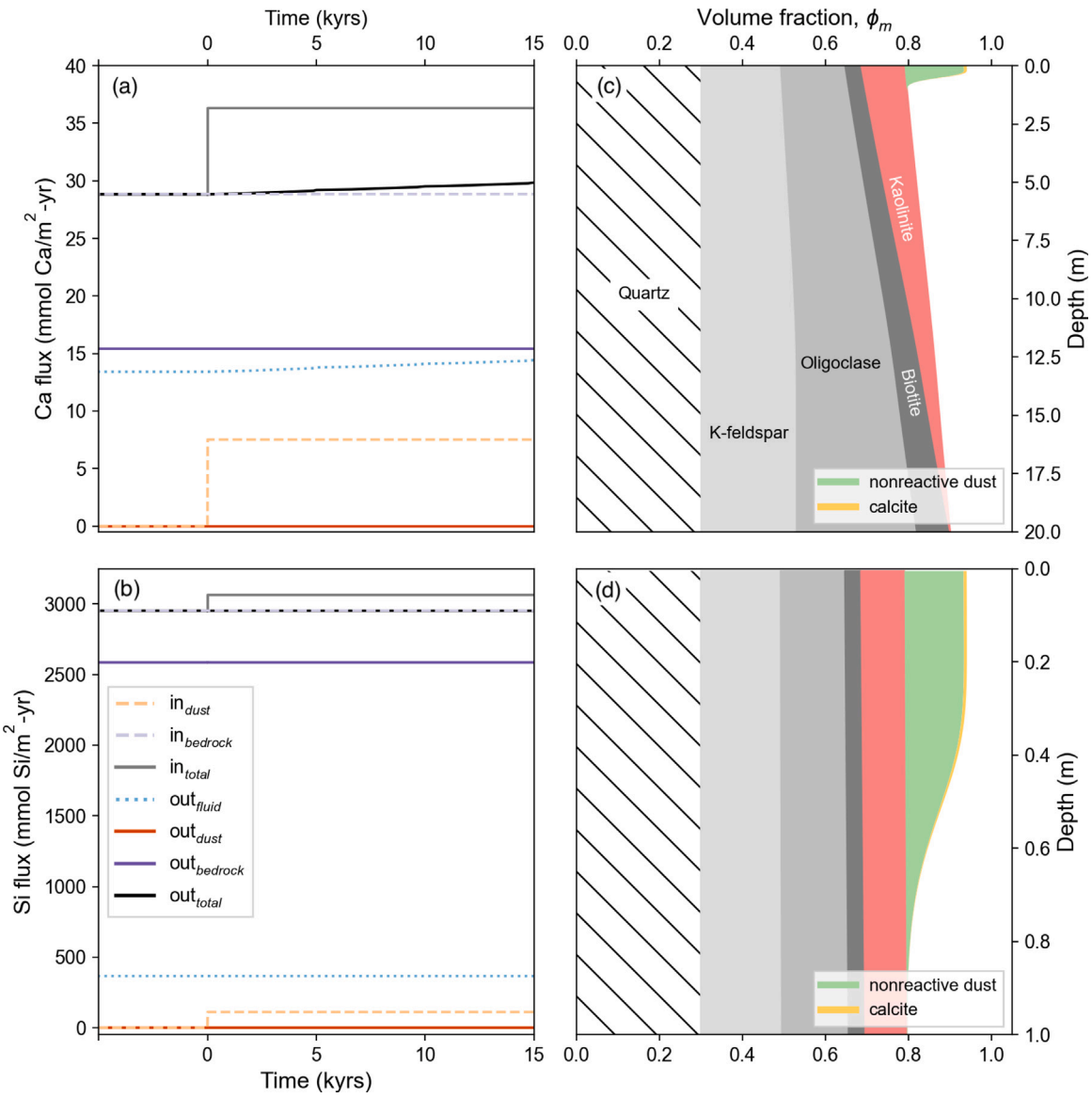

Fig. 8. Mass fluxes in and out of the domain for (a) Ca and (b) SiO_2 in the Sapine model. (c) At 15 kyr after the start of dust deposition, this new solid is observable as a component of the solid phase assemblage at the top of the domain and (d) a higher-resolution depth scale reveals that it has reached ~80 cm depth. "Nonreactive" dust refers to the fraction of the exogenous dust input composed of kaolinite, with a dissolution rate constant set to a negligibly low value to prevent reactivity in the timescale of this simulation (Table 2).

regolith's internal reactivity and weathering rates. In our RTM, quartz, oligoclase, and biotite mineral rates are constant over time since dust deposition starts (Fig. 9a), while kaolinite and K-feldspar rates decrease, most significantly at 12.5 m depth, slowing down by 1.5% and 15%, respectively (Fig. 9b). The relative decrease of the kaolinite precipitation rate is smaller than that of the K-feldspar dissolution rate because this clay is a product of the ensemble of silicate primary mineral weathering reactions (oligoclase, K-feldspar, and biotite).

4.5. Implications and opportunities

We have shown the role of Saharan dust as a supply of Ca to an upland watershed where the weathering of underlying Ca-poor granitic bedrock was insufficient to explain field observations. The role of dust as a nutrient source is well documented across a variety of terrestrial ecosystems (Aciego et al., 2017; Chadwick et al., 1999; Pett-Ridge et al., 2009a; Soderberg and Compton, 2007). Here, our contribution expands upon these studies by utilizing a multi-component RTM to demonstrate that exogenous dust inputs can also impact the internal weathering rates of regolith. Deposition of a readily reactive exogenous mass can essentially consume the reactive potential of weakly acidic infiltrating water faster than the underlying profile, leading to a reduction in the extent of internal chemical weathering. Here, the delivery of an exogenous carbonate raises pH and alkalinity, consistent with observations in nearby northeastern Spain and northern Italy (Avila and Rodà, 2002; Rogora et al., 2004). This implies that such effect of exogenous inputs on internal weathering rates is not unique to the Sapine watershed, but likely a ubiquitous feature in locations impacted by dust deposition, consistent with the hypothesis posed by Macpherson and Sullivan (2019).

Our RTM advances beyond the steady-state assumptions commonly utilized to constrain exogenous mass inputs to watersheds (Ferrier et al., 2011; Macpherson and Sullivan, 2019). Presently, our approach subjects the weathering profile to constant rates of bedrock uplift, regolith erosion, and rainwater infiltration as informed by field observations. The dust burial rate is similarly set as a constant (Section 4.3), but the initiation of this exogenous supply is explicitly treated as a departure from steady state between bedrock uplift, weathering, and

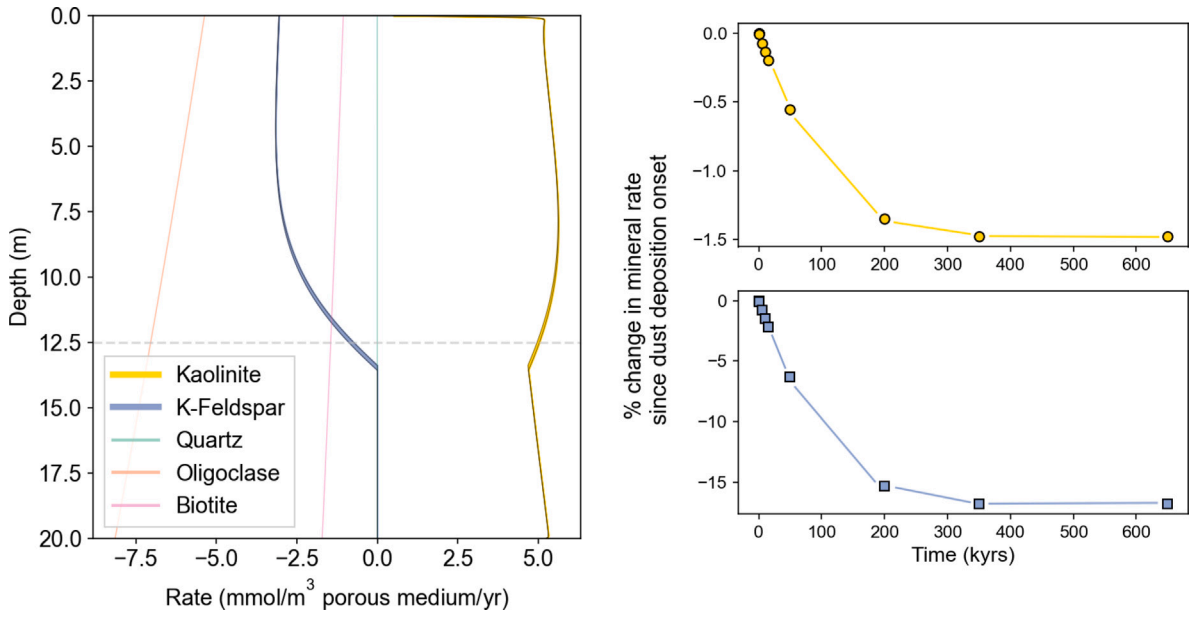

Fig. 9. (a) Range of mineral rates [mmol/m^3 porous medium/yr] from dust deposition start up to 650 kyr. (b) Percent change of mineral reaction rates for kaolinite (yellow circles) and K-feldspar (purple squares) at a depth of 12.5 m in the profile over time since dust deposition onset.

erosion. The resulting denudation of the profile is therefore no longer a simple sum of constant physical erosion and chemical weathering fluxes. Instead, a time-varying weathering flux is tracked by the numerical solution, which offers a novel means of guiding interpretation where elemental export fluxes are variable. These advancements set the stage for future treatment of combined wet and dry deposition events as they overprint internal catchment fluxes.

The present work emphasizes water-rock interactions, but the capacity exists for plant nutrient cycling to play an important role in the vertical (re)distribution of mineral-derived nutrients within the weathering profile due to uptake from the roots at depth and plant litter release and decomposition close to the surface (Druhan and Bouchez, 2024). The roots of beech trees (*Fagus sylvatica*) typically absorb elements at 30 to 50 cm depth (Berger et al., 2006; Schroth et al., 2007), and this species covers 80% of the Sapine watershed (Cognard-Plancq et al., 2001; Durand et al., 1991; Lelong et al., 1990). Elevated topsoil concentrations and depletion of rock-derived nutrients at depth could also contribute to some of the shallow elemental enrichment we see in these soil profiles. Yet fundamentally we have shown that local bedrock weathering in Sapine cannot provide sufficient calcium to agree with the totality of these observations. The extent to which vegetation dictates the balance of dust and bedrock nutrient supplies, and the capacity for vegetation to counterbalance the buffering effects of dust dissolution through carbonic acid production, proton- or ligand-promoted dissolution, or root exudation (Dontsova et al., 2020) presents an outstanding unknown. Our work offers a basis upon which to pursue these linkages via forward and process-based modeling frameworks capable of describing interactions between ecosystems and both local and exogenous rock-derived nutrient inputs under time-varying conditions.

5. Conclusions

Inputs of carbonate-bearing dust to the Mediterranean, granitic catchment of Sapine, Southern France, drive calcium (Ca) enrichment in both soils and stream water. This is shown by a suite of geochemical tracers, namely high Ca/Ti ratios in the top 80 cm of soil, elevated Ca/Na molar ratios in stream and rain waters, and departure from bedrock Sr and Nd isotopic signatures in the soils and plant litter of the site. This makes the Sapine catchment an ideal site to develop the implementation of exogenous dust as a solid phase in an reactive transport model (RTM) framework.

We developed a new functionality in the numerical RTM CrunchTope that allows for the differential movement of mineral phases. In addition to an uplifting bedrock phase moving upwards and eroding at the top of the domain, a burying dust phase was added and allowed to react while traveling downwards through the porous space. Thanks to this implementation in a previously existing RTM model developed for the Sapine watershed (Golla et al., 2024b), field observations of Ca enrichment in soils and model results are reconciled. It emerges from the RTM behavior that addition of dust to the weathering profile decreases the rates of K-feldspar dissolution and kaolinite precipitation at millennial timescales, which could have implications for the consumption of CO_2 through silicate weathering and stream solute export.

This new capability of an RTM to account for the effect of dust deposition on the composition and reactivity of a weathering profile opens the opportunity to quantify and predict the influence of exogenous inputs to catchments beyond the addition of mass and elements. We envision that this approach can also be applied to other types of solid deposition to weathering profiles, such as fertilizers or particulate pollutants, providing predictive power for the evolution of soil and stream geochemistry subject to such disturbances.

CRediT authorship contribution statement

Celia Aranda Reina: Writing – review & editing, Writing – original draft, Visualization, Investigation, Data curation. **Julien Bouchez:** Writing – review & editing, Writing – original draft, Validation, Supervision, Resources, Project administration, Methodology, Investigation, Funding acquisition, Formal analysis, Data curation, Conceptualization. **Jennifer L. Druhan:** Writing – review & editing, Writing – original draft, Visualization, Validation, Supervision, Software, Resources, Project administration, Methodology, Investigation, Funding acquisition, Formal analysis, Conceptualization.

Declaration of competing interest

The authors declare that they have no known competing financial interests or personal relationships that could have appeared to influence the work reported in this paper.

Acknowledgments

We are especially grateful to Jean-François Didon-Lescot, Jean-Marc Domergue, Nadine Grard, Didier Josselin, Philippe Martin, Yannick Manche, and Pierre-Alain Ayral for their support during fieldwork. We acknowledge the "Parc National des Cévennes" for authorizing us to conduct scientific work within the park. Funding support is provided by NSF-EAR-2047318, USA awarded to J.L.D. Sample analysis was partially supported by the CNRS National Research Infrastructure OZCAR, France ("Observatoires de la Zone Critique - Applications et Recherche") and the National Service of Observation (SNO) OHM-CV ("Observatoire HydroMétéorologique Cévennes-Vivarais"), the IPGP multidisciplinary program PARI and the Région Île-de-France SESAME 426 Grant No. 12015908, with analytical help from Marie Kuessner, Caroline Gorge, Pierre Burckel, Laëticia Faure, and Samia Hidalgo. C.A.R. acknowledges support from the Illinois Distinguished Fellowship, USA. The authors thank Marie Kuessner for initial discussions about the role of dust at Sapine, and Damien Guinoiseau for several insightful comments regarding Saharan dust composition.

Appendix A. Supplementary data

Table S1: Vegetation chemistry; Figure S1: RTM numerical dispersion analysis, Figure S2: Second moment analysis of dust diffusivity.

Supplementary material related to this article can be found online at https://doi.org/10.1016/j.gca.2025.01.023.

Data availability

Accompanying data used in this study are available with this submission and in (Golla et al., 2024c). Accompanying model files have been published on Hydroshare (Aranda Reina et al., 2025) at http://www.hydroshare.org/resource/c5411ee6e1f54b9f9c7beaa9263f6969.

References

Aciego, S.M., Riebe, C.S., Hart, S.C., Blakowski, M.A., Carey, C.J., Aarons, S.M., Dove, N.C., Botthoff, J.K., Sims, K.W., Aronson, E.L., 2017. Dust outpaces bedrock in nutrient supply to montane forest ecosystems. Nat. Commun. 8.

Anderson, S.P., Dietrich, W.E., Brimhall, G.H., 2002. Weathering profiles, mass-balance analysis, and rates of solute loss: Linkages between weathering and erosion in a small, steep catchment. GSA Bull. 114 (9), 1143–1158.

Aranda Reina, C., Bouchez, J., Druhan, J.L., 2025. Accompanying model files for Aranda Reina et al. (2025, GCA) "Quantifying the impacts of exogenous dust inputs to the critical zone using reactive transport modeling".

Avila, A., Rodà, F., 2002. Assessing decadal changes in rainwater alkalinity at a rural mediterranean site in the montseny mountains (NE Spain). Atmos. Environ. 36 (17), 2881–2890.

Bailey, S.W., Buso, D.C., Likens, G.E., 2003. Implications of sodium mass balance for interpreting the calcium cycle of a forested ecosystem. Ecol. 84 (2), 471–484.

Berger, T.W., Inselsbacher, E., Mutsch, F., Pfeffer, M., 2009. Nutrient cycling and soil leaching in eighteen pure and mixed stands of beech (fagus sylvatica) and spruce (picea abies). Forest Ecol. Manag. 258 (11), 2578–2592.

Berger, T.W., Swoboda, S., Prohaska, T., Glatzel, G., 2006. The role of calcium uptake from deep soils for spruce (picea abies) and beech (fagus sylvatica). Forest Ecol. Manag. 229 (1–3), 234–246.

Boudevillain, B., Delrieu, G., Galabertier, B., Bonnifait, L., Bouilloud, L., Kirstetter, P.-E., Mosini, M.-L., 2011. The Cévennes-Vivarais mediterranean hydrometeorological observatory database. Water Resour. Res. 47 (7).

Brichau, S., Respaut, J.-P., Monié, P., 2008. New age constraints on emplacement of the Cévenol granitoids, south french massif central. Int. J. Earth Sci. 97 (4), 725–738.

Brimhall, G.H., Dietrich, W.E., 1987. Constitutive mass balance relations between chemical composition, volume, density, porosity, and strain in metasomatic hydrochemical systems: Results on weathering and pedogenesis. Geochim. Cosmochim. Acta 51 (3), 567–587.

Capo, R.C., Stewart, B.W., Chadwick, O.A., 1998. Strontium isotopes as tracers of ecosystem processes: theory and methods. Geoderma 82 (1–3), 197–225.

Caro, G., Bourdon, B., Birck, J.L., Moorbath, S., 2006. High-precision 142Nd/144nd measurements in terrestrial rocks: Constraints on the early differentiation of the earth's mantle. Geochim. Cosmochim. Acta 70 (1), 164–191.

Celle-Jeanton, H., Travi, Y., Loÿe-Pilot, M.D., Huneau, F., Bertrand, G., 2009. Rainwater chemistry at a mediterranean inland station (avignon, France): Local contribution versus long-range supply. Atmos. Res. 91 (1), 118–126.

Chadwick, O.A., Derry, L.A., Vitousek, P.M., Huebert, B.J., Hedin, L.O., 1999. Changing sources of nutrients during four million years of ecosystem development. Nature 397 (6719), 491–497.

Chauvet, A., Volland-Tuduri, N., Lerouge, C., Bouchot, V., Monié, P., Charonnat, X., Faure, M., 2012. Geochronological and geochemical characterization of magmatic-hydrothermal events within the southern variscan external domain (Cévennes area, France). Int. J. Earth Sci. 101 (1), 69–86.

Cognard-Plancq, A.-L., Marc, V., Didon-Lescot, J.-F., Normand, M., 2001. The role of forest cover on streamflow down sub-mediterranean mountain watersheds: a modelling approach. J. Hydrol. 254 (1–4), 229–243.

Cook, B.I., Smerdon, J.E., Seager, R., Coats, S., 2014. Global warming and 21st century drying. Clim. Dyn. 43 (9–10), 2607–2627.

Croisé, L., Ulrich, E., Duplat, P., Jaquet, O., 2005. Two independent methods for mapping bulk deposition in France. Atmos. Environ. 39 (21), 3923–3941.

Derry, L.A., Chadwick, O.A., 2007. Contributions from earth's atmosphere to soil. Elements 3 (5), 333–338.

Dessert, C., Clergue, C., Rousteau, A., Crispi, O., Benedetti, M., 2019. Atmospheric contribution to cations cycling in highly weathered catchment, guadeloupe (lesser antilles). Chem. Geol. 531, 119354.

Didon-Lescot, J.-F., 1996. Foret de Developpement Durable Au Mont Lozère. Impact D'une Plantation De Resineux, De Sa Coupe Et De Son Remplacement, Sur L'eau Et Sur Les Reserves Minerals Du Sol (Ph.D. thesis).

DIGIS Team, 2023. GEOROC compilation: Rock types.

Dontsova, K., Balogh-Brunstad, Z., Le Roux, G., Chorover, J., 2020. Plants as Drivers of Rock Weathering. Technical Report.

Druhan, J.L., Bouchez, J., 2024. Ecological regulation of chemical weathering recorded in rivers. Earth Planet. Sci. Lett. 641, 118800.

Druhan, J.L., Lawrence, C.R., 2021. Development of soil radiocarbon profiles in a reactive transport framework. Geochim. Cosmochim. Acta 306, 63–83.

Druhan, J.L., Steefel, C.I., Williams, K.H., DePaolo, D.J., 2013. Calcium isotope fractionation in groundwater: Molecular scale processes influencing field scale behavior. Geochim. Cosmochim. Acta 119, 93–116.

Dupraz, C., 1984. Bilans Des Transferts D'eau Et D'elements Mineraux Dans Trois Bassins-Versants Comparatifs a Vegetations Contrastees (Mont-Lozère, France) (Ph.D. thesis). Université d'Orléans, Orléans.

Durand, P., Neal, C., Lelong, F., 1992. Anthropogenic and natural contributions to the rainfall chemistry of a mountainous area in the Cevennes National Park (Mont-Lozere, southern France). J. Hydrol. 130 (1–4), 71–85.

Durand, P., Neal, C., Lelong, F., Didon-Lescot, J.F., 1991. Hydrochemical variations in spruce, beech and grassland areas, mont lozere, southern france. Technical Report, pp. 57–70.

Fantle, M.S., Maher, K.M., Depaolo, D.J., 2010. Isotopic approaches for quantifying the rates of marine burial diagenesis. Rev. Geophys. 48 (3).

Feng, S., Fu, Q., 2013. Expansion of global drylands under a warming climate. Atmos. Chem. Phys. 13 (19), 10081–10094.

Fernandez, N.M., Bouchez, J., Derry, L.A., Chorover, J., Gaillardet, J., Giesbrecht, I., Fries, D., Druhan, J.L., 2022. Resiliency of silica export signatures when low order streams are subject to storm events. J. Geophys. Res.: Biogeosci. 127 (5).

Ferrier, K.L., Kirchner, J.W., Finkel, R.C., 2011. Estimating millennial-scale rates of dust incorporation into eroding hillslope regolith using cosmogenic nuclides and immobile weathering tracers. J. Geophys. Res. 116 (F3), F03022.

Formenti, P., Caquineau, S., Desboeufs, K., Klaver, A., Chevaillier, S., Journet, E., Rajot, J.L., 2014. Mapping the physico-chemical properties of mineral dust in western africa: Mineralogical composition. Atmos. Chem. Phys. 14 (19), 10663–10686.

Formenti, P., Schütz, L., Balkanski, Y., Desboeufs, K., Ebert, M., Kandler, K., Petzold, A., Scheuvens, D., Weinbruch, S., Zhang, D., 2011. Recent progress in understanding physical and chemical properties of african and Asian mineral dust.

Gaillardet, J., Braud, I., Hankard, F., Anquetin, S., Bour, O., Dorfliger, N., de Dreuzy, J., Galle, S., Galy, C., Gogo, S., Gourcy, L., Habets, F., Laggoun, F., Longuevergne, L., Le Borgne, T., Naaim-Bouvet, F., Nord, G., Simonneaux, V., Six, D., Tallec, T., Valentin, C., Abril, G., Allemand, P., Arènes, A., Arfib, B., Arnaud, L., Arnaud, N., Arnaud, P., Audry, S., Comte, V.B., Batiot, C., Battais, A., Bellot, H., Bernard, E., Bertrand, C., Bessière, H., Binet, S., Bodin, J., Bodin, X., Boithias, L., Bouchez, J., Boudevillain, B., Moussa, I.B., Branger, F., Braun, J.J., Brunet, P., Caceres, B., Calmels, D., Cappelaere, B., Celle-Jeanton, H., Chabaux, F., Chalikakis, K., Champollion, C., Copard, Y., Cotel, C., Davy, P., Deline, P., Delrieu, G., Demarty, J., Dessert, C., Dumont, M., Emblanch, C., Ezzahar, J., Estèves, M., Favier, V., Faucheux, M., Filizola, N., Flammarion, P., Floury, P., Fovet, O., Fournier, M., Francez, A.J., Gandois, L., Gascuel, C., Gayer, E., Genthon, C., Gérard, M.F., Gilbert, D., Gouttevin, I., Grippa, M., Gruau, G., Jardani, A., Jeanneau, L., Join, J.L., Jourde, H., Karbou, F., Labat, D., Lagadeuc, Y., Lajeunesse, E., Lastennet, R., Lavado, W., Lawin, E., Lebel, T., Le Bouteiller, C., Legout, C., Lejeune, Y., Le Meur, E., Le Moigne, N., Lions, J., Lucas, A., Malet, J.P., Marais-Sicre, C., Maréchal, J.C., Marlin, C., Martin, P., Martins, J., Martinez, J.M.,

Massei, N., Mauclerc, A., Mazzilli, N., Molénat, J., Moreira-Turcq, P., Mougin, E., Morin, S., Ngoupayou, J.N., Panthou, G., Peugeot, C., Picard, G., Pierret, M.C., Porel, G., Probst, A., Probst, J.L., Rabatel, A., Raclot, D., Ravanel, L., Rejiba, F., René, P., Ribolzi, O., Riotte, J., Rivière, A., Robain, H., Ruiz, L., Sanchez-Perez, J.M., Santini, W., Sauvage, S., Schoeneich, P., Seidel, J.L., Sekhar, M., Sengtaheuanghoung, O., Silvera, N., Steinmann, M., Soruco, A., Tallec, G., Thibert, E., Lao, D.V., Vincent, C., Viville, D., Wagnon, P., Zitouna, R., 2018. OZCAR: The french network of critical zone observatories. Vadose Zone J. 17 (1), 1–24.

Golla, J., Bouchez, J., Druhan, J., 2024a. Antecedent hydrologic conditions reflected in stream lithium isotope ratios during storms. Geophys. Res. Lett. 51 (17), e2024GL109624.

Golla, J.K., Bouchez, J., Kuessner, M.L., Druhan, J.L., 2024b. Weathering incongruence in mountainous Mediterranean climates recorded by stream lithium isotope ratios. J. Geophys. Res.: Earth Surf..

Golla, J.K., Kuessner, M.L., Reina, C.A., Grard, N., Domergue, J.-M., Ayral, P.-A., Didon-Lescot, J.-F., Bouchez, J., 2024c. Geochemistry of a weathering profile and natural waters in the upland Mediterranean catchment of Sapine, Mt-Lozère, southern France.

Gray, H.J., Keen-Zebert, A., Furbish, D.J., Tucker, G.E., Mahan, S.A., 2020. Depth-dependent soil mixing persists across climate zones. Proc. Natl. Acad. Sci. 117 (16), 8750–8756.

Guinoiseau, D., Fekiacova, Z., Allard, T., Druhan, J.L., Balan, E., Bouchez, J., 2021. Tropical weathering history recorded in the silicon isotopes of lateritic weathering profiles. Geophys. Res. Lett. 48 (19).

Guinoiseau, D., Singh, S.P., Galer, S.J., Abouchami, W., Bhattacharyya, R., Kandler, K., Bristow, C., Andreae, M.O., 2022. Characterization of saharan and sahelian dust sources based on geochemical and radiogenic isotope signatures. Quat. Sci. Rev. 293.

Hajj, F., Poszwa, A., Bouchez, J., Guérold, F., 2017. Radiogenic and "stable" strontium isotopes in provenance studies: A review and first results on archaeological wood from shipwrecks.

Hanchi, A., 1994. Cycle de L'eau Et Des Élements Biogènes Dans Un Bassin Versant Forestière: Cas D'une Hetrâie Au Mont Lozère (Ph.D. thesis).

Huber, C., Druhan, J.L., Fantle, M.S., 2017. Perspectives on geochemical proxies: The impact of model and parameter selection on the quantification of carbonate recrystallization rates. Geochim. Cosmochim. Acta 217, 171–192.

Israelevich, P., Ganor, E., Alpert, P., Kishcha, P., Stupp, A., 2012. Predominant transport paths of saharan dust over the mediterranean sea to europe. J. Geophys. Res.: Atmos. 117 (2).

Kaste, J.M., Heimsath, A.M., Bostick, B.C., 2007. Short-term soil mixing quantified with fallout radionuclides. Geol. 35 (3), 243–246.

Kim, J., 2008. Transport routes and source regions of Asian dust observed in Korea during the past 40 years (1965–2004). Atmos. Environ. 42 (19), 4778–4789.

Kuessner, M.K., 2018. The Interplay Between Chemical Weathering and Hydrology in the Critical Zone - Insights from Trace Elements and Lithium Isotopes (Ph.D. thesis). Institut de Physique du Globe de Paris, Paris.

Lawrence, C.R., Reynolds, R.L., Ketterer, M.E., Neff, J.C., 2013. Aeolian controls of soil geochemistry and weathering fluxes in high-elevation ecosystems of the Rocky Mountains, Colorado. Geochim. Cosmochim. Acta 107, 27–46.

Lehnert, K., Su, Y., Langmuir, C.H., Sarbas, B., Nohl, U., 2000. A global geochemical database structure for rocks. Geochem. Geophys. Geosyst. 1 (5).

Lelong, F., Dupraz, C., Durand, P., Didon-Lescot, J., 1990. Effects of vegetation type on the biogeochemistry of small catchments (Mont Lozere, France). J. Hydrol. 116 (1–4), 125–145.

Lequy, E., Nicolas, M., Conil, S., Turpault, M.P., 2013. Relationship between atmospheric dissolved deposition and mineral dust deposition in French forests. Water Air Soil Pollut. 224 (9).

Li, X., Fisk, M.C., Fahey, T.J., Bohlen, P.J., 2002. Influence of earthworm invasion on soil microbial biomass and activity in a northern hardwood forest. Soil Biol. Biochem. 34 (12), 1929–1937.

Loye-Pilot, M., Morelli, J., 1988. Fluctuations of ionic composition of precipitations collected in corsica related to changes in the origins of incoming aerosols. J. Aerosol Sci. 19 (5), 577–585.

Lyman, J., Fleming, R.H., 1940. Composition of sea water. J. Mar. Res..

Macpherson, G.L., Sullivan, P.L., 2019. Dust, impure calcite, and phytoliths: Modeled alternative sources of chemical weathering solutes in shallow groundwater. Chem. Geol. 527.

Mahowald, N.M., Baker, A.R., Bergametti, G., Brooks, N., Duce, R.A., Jickells, T.D., Kubilay, N., Prospero, J.M., Tegen, I., 2005. Atmospheric global dust cycle and iron inputs to the ocean. Glob. Biogeochem. Cycles 19 (4).

Malcles, O., Vernant, P., Chéry, J., Camps, P., Cazes, G., Ritz, J.F., Fink, D., 2020. Determining the plio-quaternary uplift of the southern french massif central; a new insight for intraplate orogen dynamics. Solid Earth 11 (1), 241–258.

Martin, C., Didon-Lescot, J.-F., Cosandey, C., Le, C.C., 2003. Le Fonctionnement Hydrologique Des Petits Bassins Versants Granitiques Du Mont-Lozère : Influence Du Couvert Végétal Sur Les Crues Et Les Étiages. Technical Report, URL: https://hal.archives-ouvertes.fr/hal-00312824.

Masson, C., Mazzotti, S., Vernant, P., Doerflinger, E., 2019. Extracting small deformation beyond individual station precision from dense global navigation satellite system (GNSS) networks in France and western europe. Solid Earth 10 (6), 1905–1920.

Pett-Ridge, J.C., Derry, L.A., Barrows, J.K., 2009a. Ca/Sr and 87Sr/86Sr ratios as tracers of Ca and Sr cycling in the Rio Icacos watershed, Luquillo Mountains, Puerto Rico. Chem. Geol. 267 (1–2), 32–45.

Pett-Ridge, J.C., Derry, L.A., Kurtz, A.C., 2009b. Sr isotopes as a tracer of weathering processes and dust inputs in a tropical granitoid watershed, Luquillo Mountains, Puerto Rico. Geochim. Cosmochim. Acta 73 (1), 25–43.

Pin, C., Bassin, C., 1992. Evaluation of a strontium-specific extraction chromatographic method for isotopic analysis in geological materials. Anal. Chim. Acta 269 (2), 249–255.

Prospero, J.M., Lamb, P.J., 2003. African droughts and dust transport to the Caribbean: Climate change implications. Sci. 302 (5647), 1024–1027.

Riley, J., Tongudai, M., 1967. The major cation/chlorinity ratios in sea water. Chem. Geol. 2, 263–269.

Rodriguez-Navarro, C., Di Lorenzo, F., Elert, K., 2018. Mineralogy and physicochemical features of saharan dust wet deposited in the Iberian Peninsula during an extreme red rain event. Atmos. Chem. Phys. 18 (13), 10089–10122.

Rogora, M., Mosello, R., Marchetto, A., 2004. Long-term trends in the chemistry of atmospheric deposition in Northwestern Italy: the role of increasing Saharan dust deposition. Tellus B 56 (5), 426.

Salvador, P., Pey, J., Pérez, N., Querol, X., Artíñano, B., 2022. Increasing atmospheric dust transport towards the western Mediterranean over 1948–2020. Npj Clim. Atmos. Sci. 5 (1).

Schaller, M., Ehlers, T.A., 2022. Comparison of soil production, chemical weathering, and physical erosion rates along a climate and ecological gradient (Chile) to global observations. Earth Surf. Dyn. 10 (1), 131–150.

Schroth, A.W., Friedland, A.J., Bostick, B.C., 2007. Macronutrient depletion and redistribution in soils under conifer and Northern hardwood forests. Soil Sci. Am. J. 71 (2), 457–468.

Soderberg, K., Compton, J.S., 2007. Dust as a nutrient source for fynbos ecosystems, South Africa. Ecosys. 10 (4), 550–561.

Steefel, C.I., Appelo, C.A., Arora, B., Jacques, D., Kalbacher, T., Kolditz, O., Lagneau, V., Lichtner, P.C., Mayer, K.U., Meeussen, J.C., Molins, S., Moulton, D., Shao, H., Šimůnek, J., Spycher, N., Yabusaki, S.B., Yeh, G.T., 2015. Reactive transport codes for subsurface environmental simulation. Comput. Geosci. 19 (3), 445–478.

Talbot, J.Y., Martelet, G., Courrioux, G., Chen, Y., Faure, M., 2004. Emplacement in an extensional setting of the Mont Lozère-Borne granitic complex (SE France) inferred from comprehensive AMS, structural and gravity studies. J. Struct. Geol. 26 (1), 11–28.

Uno, I., Eguchi, K., Yumimoto, K., Takemura, T., Shimizu, A., Uematsu, M., Liu, Z., Wang, Z., Hara, Y., Sugimoto, N., 2009. Asian dust transported one full circuit around theglobe. Nat. Geosci. 2 (8), 557–560.

Vincent, J., Laurent, B., Losno, R., Bon Nguyen, E., Roullet, P., Sauvage, S., Chevaillier, S., Coddeville, P., Ouboulmane, N., di Sarra, A.G., Tovar-Sánchez, A., Sferlazzo, D., Massanet, A., Triquet, S., Morales Baquero, R., Fornier, M., Coursier, C., Desboeufs, K., Dulac, F., Bergametti, G., 2016. Variability of mineral dust deposition in the western Mediterranean basin and south-east of France. Atmos. Chem. Phys. 16 (14), 8749–8766.

White, P.J., Broadley, M.R., 2003. Calcium in plants. Ann. Botany 92 (4), 487–511.

Xu, Y., Dessert, C., Losno, R., 2022. Atmospheric deposition over the Caribbean region: Sea salt and Saharan dust are sources of essential elements on the Island of Guadeloupe. J. Geophys. Res.: Atmos. 127.

Yeghicheyan, D., Aubert, D., Bouhnik-Le Coz, M., Chmeleff, J., Delpoux, S., Djouraev, I., Granier, G., Lacan, F., Piro, J.-L., Rousseau, T., Cloquet, C., Marquet, A., Menniti, C., Pradoux, C., Freydier, R., Vieira da Silva-Filho, E., Suchorski, K., 2019. A new interlaboratory characterisation of silicon, rare earth elements and twenty-two other trace element concentrations in the natural river water certified reference material SLRS-6 (NRC - CNRC). Geostand. Geoanalytical Res. 43 (3), 475–496.

Yeghicheyan, D., Bossy, C., Bouhnik Le Coz, M., Douchet, C., Granier, G., Heimburger, A., Lacan, F., Lanzanova, A., Rousseau, T.C., Seidel, J.L., Tharaud, M., Candaudap, F., Chmeleff, J., Cloquet, C., Delpoux, S., Labatut, M., Losno, R., Pradoux, C., Sivry, Y., Sonke, J.E., 2013. A compilation of silicon, rare earth element and twenty-one other trace element concentrations in the natural river water reference material SLRS-5 (NRC-CNRC). Geostand. Geoanalytical Res. 37 (4), 449–467.

Yoo, K., Ji, J., Aufdenkampe, A., Klaminder, J., 2011. Rates of soil mixing and associated carbon fluxes in a forest versus tilled agricultural field: Implications for modeling the soil carbon cycle. J. Geophys. Res.: Biogeosci. 116 (1).

Zielhofer, C., von Suchodoletz, H., Fletcher, W.J., Schneider, B., Dietze, E., Schlegel, M., Schepanski, K., Weninger, B., Mischke, S., Mikdad, A., 2017. Millennial-scale fluctuations in saharan dust supply across the decline of the African humid period. Quat. Sci. Rev. 171, 119–135.